2018-01-01

Additive Manufacturing Of Energy Harvesting Material System For Active Wireless Mems

Victor Fernando Elicerio
University of Texas at El Paso, vfelicerio@miners.utep.edu

ADDITIVE MANUFACTURING OF ENERGY HARVESTING MATERIAL SYSTEM FOR ACTIVE WIRELESS MEMS

VICTOR FERNANDO ELICERIO

Master's Program in Mechanical Engineering

APPROVED:

David Espalin, Ph.D., Chair

Yirong Lin, Ph.D.

David A. Roberson, Ph.D.

Charles Ambler, Ph.D.
Dean of the Graduate School

Dedication

I dedicate this thesis to my family Fernando Elicerio, Julissa Elicerio, Iris Elicerio, and April Marie Reza. Thank you for believing in me.

ADDITIVE MANUFACTURING OF ENERGY HARVESTING MATERIAL SYSTEM FOR ACTIVE WIRELESS MEMS

by

VICTOR FERNANDO ELICERIO, B.S.M.E.

THESIS

Presented to the Faculty of the Graduate School of

The University of Texas at El Paso

in Partial Fulfillment

of the Requirements

for the Degree of

MASTER OF SCIENCE

Department of Mechanical Engineering

THE UNIVERSITY OF TEXAS AT EL PASO

May 2018

Acknowledgements

I would like to thank Dr. David Espalin and Dr. Ryan Wicker, the Research director and Director of the W.M. Keck Center for 3D Innovation, respectively, for the opportunity to learn and grow as a student both in my graduate and undergraduate career at The University of Texas at El Paso (UTEP). The guidance and knowledge offered at the W.M. Keck Center for 3D Innovation is unparalleled and the research conducted would not be possible without the amazing facility that I have had the opportunity to work in for the duration of my academic career. Furthermore I would like to thank Jorge Mireles and Jose Gonzalez who were not only mentors to me in the realm of additive manufacturing, but also my friends.

I would like to thank Dr. Yirong Lin who served as a mentor throughout the research process and allowed me to exceed my own expectations as to what I am able of accomplishing. I show my utmost thanks and appreciation to Luis Chavez, who assisted me in all facets of the project and essentially taught me everything that I know about energy harvesting systems. I owe thanks to the research team assembled by Dr. Lin who also assisted me throughout the research. I would also like to thank the U.S. Department of Energy, Fossil Energy Research, University Coal Research (UCR), Historically Black Colleges and Universities (HBC), and Other Minority Institutions (OMI) for the support to perform the research conducted.

I would like to thank my family, whose support throughout this journey has continuously encouraged me to be a better version of myself. Finally, I owe a very special thank you to April Marie Reza, whose love and support has guided me through the most difficult parts of this journey and will always be my reason to strive for greatness.

Abstract

Additive manufacturing (AM – most commonly known as 3D printing) is a fabrication method and aims to increase production efficiency while lowering costs of constructing quality components for industry application when compared to traditional machining. In addition to this, AM possesses capabilities that far exceed machining as complex geometries are achievable through an array of technologies in a wide variety of materials. The AM process begins with a computer aided design (CAD) which creates a design path for a 3D printer to follow. By following this path, components are built from bottom to top in a layer by layer fashion. Binder jetting (BJ) is an AM process that adheres each layer of the constructed object together with a liquid binder solution jetted through a print head. Once fabricated, components are subjected to heat treatments to further adhere particles within each layer to achieve higher densities. What separates BJ from other methods of AM are its capabilities to fabricate utilizing materials that normally require casting such as sands and ceramics. In addition to this BJ also possesses the capability to fabricate a variety of metals and alloys, such as copper and Inconel alloys.

Recently in the field of energy harvesting, micro electrical mechanical sensors (MEMS) have garnered substantial interest due to the growing demand for green energy production from self-sufficient systems. A proposed method for the production of these self-sufficient sensors uses piezoceramic materials, which produce electrical charges upon excitation. Harvesting benign energy via piezoelectric materials is a cost effective alternative to batteries normally utilized in these wireless sensors as batteries often require replacement and routine maintenance. The challenges with implementation of these wireless MEMS within energy generating systems is the small amount of energy produced from material excitation and whether this energy supply will sustain a sensor for an extended period of time. The research conducted aims to produce AM fabricated piezoceramics capable of producing adequate energy outputs from several variants of excitation via a custom test set up.

BJ is selected as the AM technology utilized for component fabrication as this technology allows for the fabrication of piezoceramics without diminishing the piezoelectric characteristics of materials throughout the manufacturing process. Throughout this component fabrication process, several variants of piezoelectric materials were investigated as high energy output and high density from components were desired due to the nature of the harsh environment MEMS are subjected to in the fossil energy industry. Pure barium titanate (BTO), pure lithium niobate ($LiNbO_3$), pure lead zirconate titanate (PZT), a mixture of PZT & BTO, and a mixture of $LiNbO_3$ & graphene oxide (GO) were all iterations of piezoelectric materials that were printed on the ExOne M-Lab BJ printer for this work. Prior to implementing these materials within the printer, the feasibility of each iteration of material was tested via pellet fabrication. These samples were fabricated by depositing the powder material and binder in a casting to simulate a printed component. From this, the mixture was packed together using 3000N of compressional force from a hydraulic press which provided a high density green body component. Heat treatments applied to these samples achieved high density (in the range of 57% to 94% full theoretical density) for each material iteration, thus producing a target density for AM fabricated components to attain. Furthermore, contact angle measurements were also performed prior to printing which determined the wettability of the binder solution when applied to the piezoelectric material. From this test the contact angle of pure and doped binder solution revealed that binder with weight concentrations of up to 1% GO maintain hydrophilic qualities, therefore allowing all iterations of binders to be investigated in the AM process.

To harvest a sufficient supply of energy for the proposed MEMS, the feasibility of subjecting a piezoelectric material to combined excitations for producing doubled amounts of power was tested on a solid PZT-5A sample purchased from a manufacturer. The pyroelectric and piezoelectric characteristics of this material allow for energy production from mechanical and thermal excitation. Therefore a custom test setup to implement thermal and mechanical stress upon the material simultaneously was designed and utilized to determine the energy yield produced from coupled excitation. The setup consisted of a parallel synchronized switch harvesting on the

inductor (SSHI) rectifying circuit to harvest energy produced, a custom load frame fixture compatible with an INSTRON 8801 load frame to apply compressional stress, and 60 W resistive heating cartridges for thermal stress application upon the sample. To ensure the feasibility of this energy harvesting investigation a total of five test parameters were assessed. Cyclical compression-compression loadings of 3500N were applied to the sample for a pure mechanical test and cyclical thermal loadings fluctuating in the range of 50°C-60°C were applied to the sample for pure thermal testing. The sample was then secured within the fixture with 2500N of compressional force and subjected solely to 50°C for a pure thermal test and then repeated at a temperature of 60°C to determine if higher temperatures yielded more power production. Finally the sample was subjected to 3500N of cyclical mechanical loading simultaneously with thermal fluctuations between 50°C-60°C for combined energy harvesting. This investigation revealed although combined energy harvesting is feasible, pure thermal stress applications were dominant when coupled with mechanical stress frequencies. Pure mechanical loadings yielded powers in the range of 200 nW whereas pure thermal loadings yielded powers in the range of 500 nW. Furthermore, the investigation proved that increased pure thermal stress concentrations yield the highest power amongst other test iterations.

From these preliminary investigations the feasibility of additively manufacturing piezoceramics was confirmed and parameter development for fabrication ensued. Due to correlations between mechanical strength and parameters such as high binder saturation, low layer thickness, and low powder roller speed, each iteration of material was subjected to processing parameters that would produce relatively higher density components. Once fabricated, each material also possessed specific heat treatment parameters to avoid material oxidation or melting while pursuing full density. Regardless of these specific parameters, full density was not attainable from AM fabricated components, with the highest recorded density belonging to the PZT & BTO iteration of powder, the porous component achieved 58% of the full theoretical density. Other materials such as pure $LiNbO_3$ and pure BTO yielded densities such as 39.4% and 57.9%, respectively.

The low density of components did not allow for piezoelectric property measurement, however the PZT & BTO was an exception. After being thermally poled at 120°C in a non-conductive silicon oil with a static electric field of 1.2 kV/mm, the d33 measurement was 3 E^{-12}C/N (pico-newton). In comparison to a pellet sample comprised of this mixture yielding 70 pico-newton, and a pure PZT pellet sample yielding 500 pico-newton, the piezoelectricity of the AM fabricated sample was low. This was attributed to high porosity of the AM fabricated components. In the pursuit of a higher density from these components to produce higher piezoelectric characteristics, further process parameter development in the BJ stage was executed.

Table of Contents

Acknowledgements v

Abstract vi

Table of Contents x

List of Tables xii

List of Figures xiii

Chapter 1: Introduction 1

1.1 Background 1

1.2 Thesis motivation 2

1.3 Thesis outline 3

Chapter 2: Literature review 5

2.1 Additive manufacturing 5

2.2 Binder jetting 7

2.3 Additive manufacturing of ceramic materials 10

2.4 Sintering of ceramic materials 12

2.5 Piezoelectric materials 14

2.6 Thermal energy harvesting 16

2.7 Mechanical energy harvesting 18

2.8 Combined energy harvesting 19

Chapter 3: Materials & methods 21

3.1 Piezoelectric materials 21

3.2 Binder preparation 24

3.3 Binder characterization 25

3.4 Powder mixing 26

3.4.1 $LiNbO_3$ & GO 26

3.4.2 BTO & $LiNbO_3$ 26

3.4.3 PZT & BTO 29

3.5 Pellet sample fabrication 29

3.6 Piezoelectric measurement 31

3.7 Additive manufacturing of piezoelectric materials 34

3.7.1 Starting new materials....34
3.7.2 Saturation test....35
3.7.3 Powder set up....36
3.8 Additive manufacturing process parameters....36
3.9 Heat treatment of samples....40
3.10 Density measurements....42
3.11 Energy harvesting....43
3.11.1 Introduction....43
3.11.2 Rectifying circuit design....44
3.11.3 Load frame fixture fabrication....45
3.11.4 Energy harvesting testing....47
Chapter 4: Experimental results & discussion....51
4.1 BJ process parameter development....51
4.2 Density results....53
4.3 SEM & XRD....54
4.4 Piezoelectric property measurement....61
4.5 Combined energy harvesting results....63
4.5.1 Pure mechanical loading results....63
4.5.2 Pure thermal loading results....65
4.5.3 Combined loading results....66
Chapter 5: Conclusions....69
5.1 Recommendations for future work....69
5.2 Conclusions....70
Bibliography....72
Vita 78

List of Tables

Table 1 BJ process parameters dependable upon powder particle size and binder saturation..... 10
Table 2 Material properties of $LiNbO_3$ powder..... 22
Table 3 Material properties of BTO powder. 22
Table 4 Material properties of PZT powder. 23
Table 5 Material properties of PZT-5A sample..... 23
Table 6 Material properties of GO aqueous solution..... 24
Table 7 PZT & BTO BJ processing parameters 38
Table 8 $LiNbO_3$ & GO BJ processing parameters..... 39
Table 9 $LiNbO_3$ & BTO BJ processing parameters..... 40
Table 10 BJ print processing parameters..... 52
Table 11 Density measurements for each material component iteration..... 54

List of Figures

Figure 1 Schematic diagram of BJ machine. 2
Figure 2 AM technologies. 7
Figure 3 BJ process flow chart. 9
Figure 4 Inversina 2L powder mixing mechanism. 28
Figure 5 YE2730A d33 meter used for determining piezoelectricity of samples. 33
Figure 6 Thermal poling setup for PZT samples. 34
Figure 7 $LiNbO_3$ & BTO mixture sintering profile. 41
Figure 8 PZT & BTO mixture sintering profile. 42
Figure 9 $LiNbO_3$ & GO mixture sintering profile. 42
Figure 10 Finalized CAD design for custom load frame fixtures. 44
Figure 11 SSHI parallel rectifying circuit and components. 45
Figure 12 FEA results for bottom attachment of load frame fixture. 47
Figure 13 Load frame test set up utilized for energy harvesting testing. 49
Figure 14 Schematic diagram of circuit for current and power measurement. 50
Figure 15 Contact angle of each iteration of binder. A.) Pure binder, B.) 5% weight GO, C.) 10% weight GO, D.) 15% weight GO. 53
Figure 16 A.)SEM image of pure $LiNbO_3$ powder. B.) SEM image of pure BTO powder. C.) SEM image of pure PZT powder. D.) SEM image of $LiNbO_3$ & GO powder mixture. 57
Figure 17 A.) SEM capture of BJ fabricated pure BTO sample after sintering. B.) SEM capture of pure $LiNbO_3$ after sintering. C.) SEM capture of pellet $LiNbO_3$ & GO mixture after sintering. D.) SEM capture of PZT & BTO sample after sintering. 58
Figure 18 XRD analysis of pure PZT pellet sample. 59
Figure 19 XRD analysis of PZT & BTO mixture searching for traces of BTO. 60
Figure 20 XRD analysis of PZT & BTO mixture not tracing BTO. 61
Figure 21 Dielectric constants of BTO & GO pellet samples. 63
Figure 22 Voltage response to pure mechanical load application. 64
Figure 23 Rectified voltage generated from pure mechanical stress across varying resistance loadings. 65
Figure 24 Power output across varying resistances upon pure mechanical loading conditions. 65
Figure 25 Voltage response from sample upon pure thermal loading application. 66
Figure 26 Voltage output of the sample for each of the five testing conditions across each resistive loading. 67

Figure 27 Power output of the sample for each of the five testing conditions across each resistive loading. 68

Chapter 1: Introduction

1.1 Background

Additive manufacturing (AM) is a cost effective fabrication tool at low volumes that has been utilized since its invention in the 1980's to compose complex geometries that would otherwise require a strenuous procedure following traditional manufacturing techniques. Best known as 3D printing, this layer by layer manufacturing process has minimal boundaries as to what can be designed as components are created through computer aided design data which can easily be directly printed from this technology. Furthermore, due to the array of available technology capable of producing additively manufactured components, a variety of materials ranging from polymers, to metals, to composites are accessible for printing. Additively manufactured components have been implemented in industry applications in the form of functional prototypes, medical instruments, and micro-electrical mechanical systems for energy solutions. With its continuous rapid growth, AM technology advances, its range of materials broadens, and its eventual commercialization comes closer to application in all industries.

Leading the charge to commercialization, technologies such as BJ allow for the manufacturing of components comprised of materials that are typically fabricated via casting such as sand, metals, and ceramics. BJ is a technology that fabricates components from bottom to top in a layer by layer fashion, binding each layer together with an aqueous or solvent based adhesive. Once the final layer of powder has been spread, the built up component is subjected to a variety of heat treatments dependent upon the desired material properties, in order to increase component density. Organizations such as ExOne specialize in BJ technology, developing variants of binders, materials, and 3D printing systems to further enhance this method of fabrication. For this research, ceramic materials possessing both piezoelectric and pyroelectric properties were implemented within a BJ system provided by ExOne for component fabrication. Process parameters for these components were manipulated via the ExOne M-Lab printer to produce components. From this

fabrication, it was desired to obtain full density components for exposure to thermal and mechanical loadings. A schematic diagram of a BJ system is shown in Figure 1.

Energy harvesting is an alternative method for power generation that is both ubiquitous and benign. Typically, energy generated from power producing sources is not entirely used and is often lost as waste heat or vibrational energy. Energy harvesting utilizes all of this lost energy and provides a cost effective alternative to battery usage by removing factors such as maintenance and replacement. Energy harvesting can be achieved from a large variety of sources, however in this research, thermal and mechanical energy was the focus as piezoelectric and pyroelectric materials were materials subjected to variants of stress. Upon thermal and mechanical stress, these materials produced an excitation, thus inducing an output voltage that can be harvested as power.

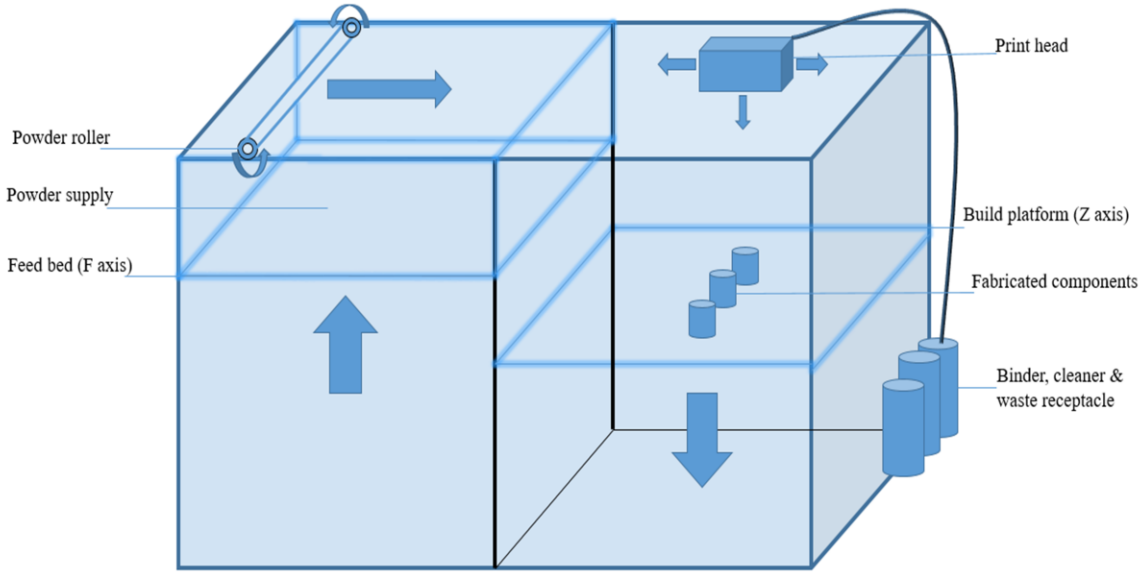

Figure 1 Schematic diagram of BJ machine.

1.2 Thesis motivation

Currently worldwide, 1.2 billion tons of coal are burned per year making it the world's top source of energy in the year 2017 [1]. By utilizing coal and natural gas as the primary sources of energy generation, substantial increases in harmful CO_2 emissions are continuously growing at an alarming rate. Growing demands for both efficient and environmentally benign power have

increased, generating extensive research interest for viable solutions. Currently in the fossil energy industry, turbines are a key component for efficiently generating energy and electricity. Within these turbine systems wireless sensors are necessary to monitor processing temperatures which in turn monitor the overall health and efficiency of the systems. In order to power these wireless sensors however, batteries are a primary source of power, which require maintenance and often need to be replaced. In order to bypass the issues that coincide with the implementation of batteries within these turbine systems, research to develop an energy harvesting system to harvest thermal and mechanical energy and convert them to electrical energy to power these wireless sensors was conducted. Therefore, the main motivation behind this research will entail providing a viable solution to increase the efficiency of energy generation and assist in the reduction of natural resources utilized to produce electrical energy. Furthermore, the target objective supporting this motivation lies within the fabrication of an energy harvesting material system using AM technology. Due to the versatile range of materials available in AM, it was feasible to fabricate an energy harvesting device capable of working up to 1200 °C to harvest both vibrational and thermal energy for powering high-temperature wireless MEMS sensors.

1.3 Thesis outline

The conducted research is described in the remaining four chapters of this work. Chapter 2 will provide an overview of all key subjects regarding the research conducted. These subjects include AM as well as other related topics such as BJ technology, AM with ceramic materials, and sintering of ceramic materials. In addition to covering the AM fraction of the research, this chapter also covers topics related to energy harvesting such as piezoelectric materials, thermal, mechanical, and combined energy harvesting. Chapter 3 describes both materials utilized and the methods in which the research was executed. This description begins with pellet fabrication to measure the feasibility of materials, moves forward to discussion of the AM process, then interprets heat treatments applied to the samples. Finally, the method of a combined energy harvesting test set up and process is discussed. Chapter 4 reviews the results obtained regarding

density measurement values, metallographic results, piezoelectric measurements, and combined energy harvesting test results. Finally chapter 5 provides conclusive findings from the works conducted and discusses recommendations for future work in this realm of research.

Chapter 2: Literature review

2.1 Additive manufacturing

As stated by ASTM committee F42, AM is a layer by layer fabrication process which joins together materials to manufacture 3D components from computer modeled data [2]. This innovative process defies opposing conventional subtractive manufacturing techniques and has been proclaimed as the future of component fabrication. The AM process begins with the creation of a computer aided design (CAD) utilizing software such as AutoCAD or SolidWorks. Upon completion, the CAD design is converted to a standard tessellation language file (STL file), which is the standard format for transferring the data of each surface of the 3D model from software to printer [3]. Once the STL file is input into the printer, specific fabrication instructions are formulated to mathematically slice the geometry and generate printing paths which allows the printer to determine process parameters for the component's layer by layer composition [4]. Each technology follows its respective method of fabrication once a print job is initialized, however, for almost all AM processes once a component is completed, post processing for consumer presentation is performed. Through advancements of this process AM not only continues to widen its spectrum of applications, but also decreases production costs as a result of shortening the design to manufacturing process [5]. Although AM may appear as one large entity, several facets of the technology can be categorized into sub divisions, separating the various technologies by method of job execution. Some of these technologies and their respective classifications can be observed in Figure 2. Technologies that specialize in manufacturing polymer based components are most commonly known by their trade-marked name and include fused deposition modeling (FDM), stereolithography (SLA), and selective laser sintering (SLS). These methods of fabrication cater to industries that rely on mostly plastic components whereas technologies such as selective laser melting (SLM), electron beam melting (EBM), direct metal laser sintering (DMLS), and BJ cater towards industries that produce metal and ceramic components [6]. As previously mentioned only specific materials coincide with their respective fabrication technology, and although the list of materials capable of being processed may seem short, researchers continue to develop methods to

bypass these obstacles. Recently, AM researchers have successfully produced components comprised of thermo-plastic/thermo-setting polymers such as ABS, metals such as stainless steel, ceramics such as alumina, uniform composites such as polymer-metal short fiber reinforced composites, and functionally graded materials such as PZT [7]. AM research continues to advance and broaden its range of materials, guiding the fabrication method toward the eventual commercialization of technology in industry application. Furthermore, several approaches towards fabrication have evolved since the principle of AM came about and each approach is catered toward a specific industry. In the automotive, aerospace, and medical industries, manufacturers take advantage of the ability to design complex geometries and benefit from AM as a cost effective approach to create custom high performance components with mechanical functionality [8]. Today, AM research aims toward meeting societal demands for continuous advancement of technology by implementing AM as a solution for practical instances such as producing fiber reinforced composites to enhance mechanical properties of geometries, bio-manufacturing to produce alternatives for non-living organs and defects within the human body, even development of micro-electrical mechanical systems for energy efficiency solutions much like the intended purpose of this work [9] [10] [11].

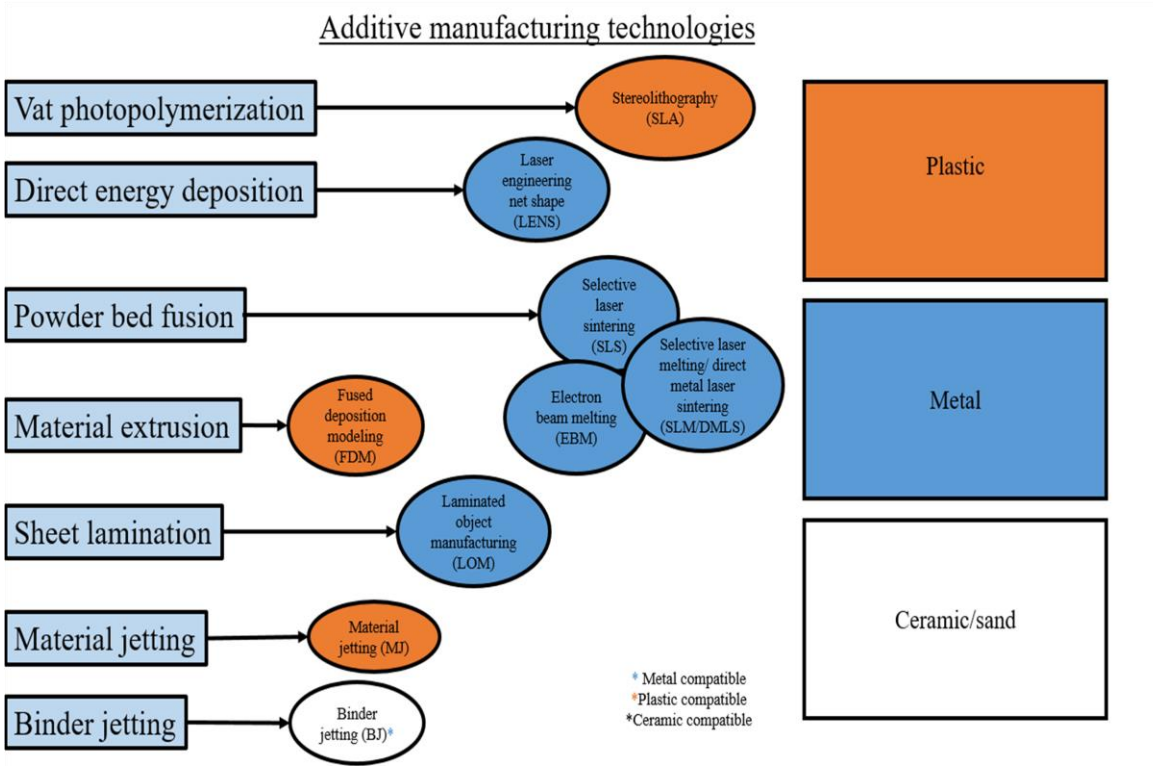

Figure 2 AM technologies.

2.2 Binder jetting

BJ is an AM technology developed at MIT in the 1990's and is described as a process in which a 3D object is fabricated by a print head depositing a binder solution into a powder bed, adhering the component together in a layer by layer fashion [12]. As with other AM processes, BJ uses a CAD file to represent a geometry, which is sliced into layers and used to produce machine fabrication instructions. Visual representation of the process flow utilized in BJ can be observed in Figure 3. Once developed, fabrication instructions are uploaded into the printer to begin the printing process. During fabrication, powder from a feeding reservoir is spread by a roller mechanism over a build platform that is lowered by a supporting piston mechanism in conjunction to the layer size of the build. This allows a new layer of powder to be spread over the old after each selective layer of binder is jetted upon the powder bed and the binder has been dried to an extent adhering the completed layers to one another. The process repeats itself until a green body (raw component comprised of glued material particles) is achieved. Heat treatments are then

performed to further densify the component and enhance its mechanical properties [13]. The following outline of the BJ process is presented to further simplify the fabrication of an AM component [14];

- Printing: A print head jets binder upon a powder bed to build up a 3D model in a layer by layer fashion.
- Curing: The liquid binder solution residing between particles in the fabricated 3D object is allowed to crosslink and harden through heat application.
- De-powdering: Excess powder not included in the original CAD file geometry is removed.
- Sintering/Infiltration: Pores coalesced within the geometry via extreme heat application for extended time periods or external liquid material permeation for enhanced material properties.
- Annealing: Internal stresses are thermally relieved.
- Finishing: Cosmetic enhancements are made such as polishing.

Process parameters for each of the aforementioned steps vary depending on materials utilized. Materials for BJ are processed in powder form and range from a variety of polymers, ceramics, metals, alloys, and sand usually distributed by companies that specialize in BJ technology such as ExOne [15], [16]. Depending on the powder particle size of the material, parameters such as layer thickness, feed ratio, roller speed, and spread speed must be taken into consideration to avoid obstruction of layers that leads to an unsuccessful build. Binder saturation levels are also tied in with particle size and can have substantial effect on heating power, drying time, curing temperature, and the sintering profile which densifies the final component [17]. Table 1 displays fabrication process parameters and their dependability upon one another. Furthermore, once densification is achieved, BJ is useful for medical and architectural prototypes and has shown versatility due to the range of materials compatible with the systems, along with reduced printing times and affordability with the costs of BJ systems averaging $20,000 USD [18]. It can also be said that BJ is energy efficient when compared to laser-based manufacturing techniques. In fact direct metal laser sintering (DMLS) consumes more than 15 times the amount of energy per minute

for fabrication than other traditional 3D printing methods [19]. In a study conducted by Xu (*et al.* 2014), a model was created by summing the consumed energy of all BJ sub processes to optimize process parameters. From this study, two sets of cylinders of equal radius and layer thickness were oriented at 0° and 90° then manufactured. It was discovered that the component oriented at 0° consumed 515.29 KJ of energy and the component oriented at 90° consumed 408.61 KJ of energy, showing that the energy consumed can be manipulated through job parameters and the BJ AM process is energy efficient when compared to laser based technologies such as DMLS that can consume up to 115,200 KJ per hour [20]. Although there are many benefits to BJ, due to limited research being reported on this technology, researchers have run into similar issues of porosity in BJ printed components. Even after sintering of components, there still remain porous areas of components where weak connections between powder particles lead to lower Young's modulus and other lowered mechanical properties [21]. Nevertheless, studies continue to improve and the range of materials for BJ research broadens routinely.

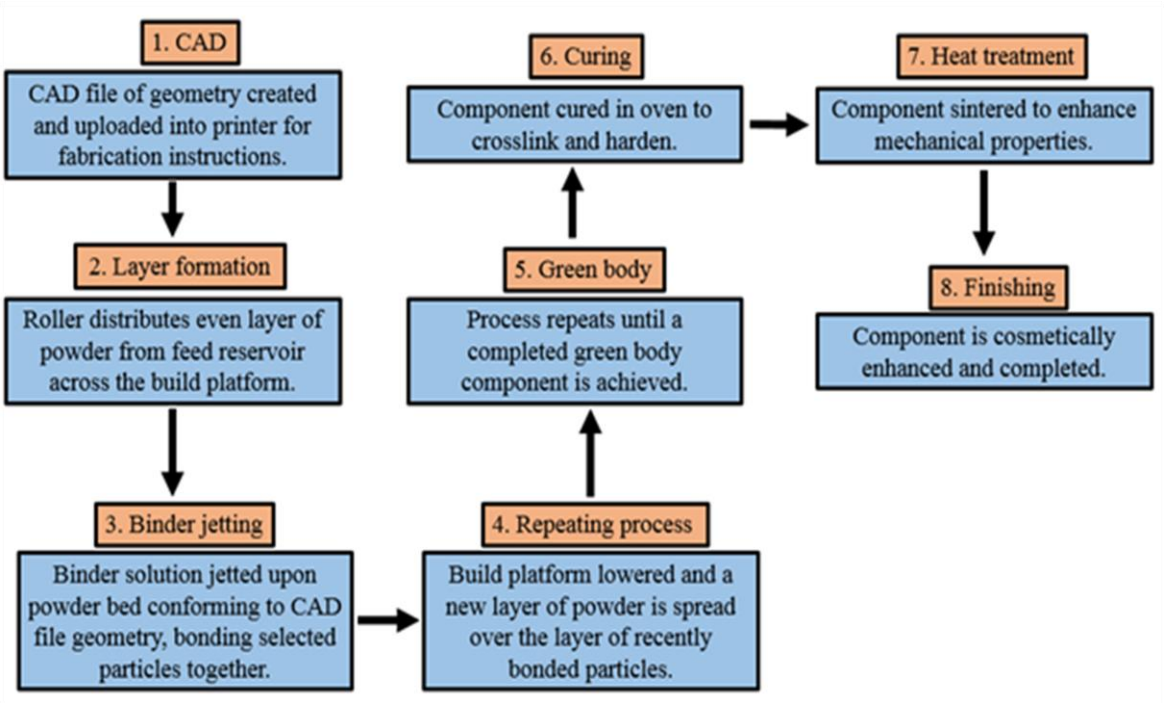

Figure 3 BJ process flow chart.

Table 1 BJ process parameters dependable upon powder particle size and binder saturation.

Binder jetting process parameters		
	Affected by particle size	Affected by binder saturation %
Layer thickness	X	
Feed ratio	X	
Roller speed	X	
Roller traverse speed	X	
Spread speed	X	
Powder packing rate (PPR)	X	
Heating power		X
Drying time		X
Total print time	X	X
Binder utilized	X	X
Cleaner utilized	X	
Waste collected	X	
Curing (time & temperature)		X
Sintering (time & temperature)		X

2.3 Additive manufacturing of ceramic materials

Ceramic components offer a unique set of material properties that are beneficial toward engineering and medical disciplines such as thermal durability, compressional mechanical strength, thermal conductivity, hardness, and chemical stability. While these materials host many unique attributes, aspects of the traditional fabrication processes (casting, molding, or machining), including the shaping of complex geometries, batch preparation, and post processing are strenuous tasks that can be costly, inspiring research to develop alternative methods of manufacturing [22].

AM of ceramic materials is one alternate fabrication method which presents a unique approach that is efficient and cost effective in comparison to traditional manufacturing techniques. Several AM processes have been used in attempt to produce ceramic components including laser sintering (LS), stereolithography (SL), laminated object manufacturing (LOM), BJ, and filament extrusion technologies such as fused deposition modeling (FDM) [23]. Ceramic materials are prone to creep and crack propagation during densification especially when implementing experimental fabrication methods. As a result of limited research conducted on the subject matter, unique obstacles such as materials being susceptible to extreme melting temperatures and high porosity in fabricated components have yet to be overcome [24]. Preliminary powder preparation techniques such as powder synthesis, are a result of researchers enhancing the material properties of the powder to produce a completed component while avoiding these aforementioned issues [25]. In a study conducted by Shahzada (*et al.* 2013), high density components are produced through innovative powder preparation techniques where composite polypropylene–alumina powder is synthesized by dissolving the powder in xylene in an inert atmosphere. Once synthesized, indirect selective laser sintering (SLS) is used to produce green bodies with 34% theoretical density (TD) which ultimately are sintered and pressure infiltrated to 89% TD with inhibited particle fracture and decreased agglomerate formation [26]. In addition to powder preparation, applications of lasers in the AM fabrication process have resulted in methods to prevent porous structures while eliminating portions of traditional post processing such as de-binding components and heat treatments that significantly induce shrinkage [27]. In fact, in a study conducted by Niu (*et al.* 2016), direct fabrication of thin walled ceramic structures comprised of an Al_2O_3/YAG mixture display excellent material properties such as a density (98.6% TD) and a micro-hardness (17.35 GPa) via a high density laser [28]. The implementation of this high density laser proved to achieve a high density while bypassing post processing heat treatments, providing a possible alternative solution to traditional fabrication methods. This fabrication method however does result in some cracking in pure ceramics due to internal stress as a function of the material's tolerance to elevated temperatures. Although fabrication by means of laser-based powder bed fusion technologies are

cost effective in the sense that the binding of layers is achieved through the extreme temperatures of the laser, several case studies conducted prove that other powder bed fusion techniques are successful in producing high density components. Furthermore, non-metal, ceramic materials such as aluminum oxide (Al_2O_3), compatible with the aforementioned technologies such as BJ, have been processed to reach up to 96% density with manipulation of build parameters such as saturation, layer thickness, and feed ratio [29]. Much like the study conducted by Gaytan (*et al.* 2015) where BJ manufactured BTO components feature properties such as a d33 value of 74.1 and a maximum relative theoretical density of 65% [30], the study conducted in this work aims to match or enhance characteristics of traditionally manufactured ceramic materials through the aid of BJ AM technology.

2.4 Sintering of ceramic materials

Sintering is described as a process of joining together individual particles through heat application, while avoiding melting the particles, to accomplish densification [31]. Furthermore, the sintering process has been deemed as the preferred method for manufacturing industrial ceramics as capillary forces are able to eliminate inter-particle pores that weaken the mechanical properties within components [32]. When sintering a component, a profile must be developed in order to determine the amount of time and temperature that the material will be subjected to heat application. This profile is dependent upon the characteristics of the material such as Curie temperature and chemical reactions produced when the material is subjected to heat. In a study conducted by Ruys (*et al.* 1995), mechanical properties of hydroxyapatite were quantified through similar sintering profiles at various temperatures below the material melting point of 1400 °C. In this study, necessary steps in the sintering process adhering to the material properties of hydroxyapatite such as implementing an inert pressurized argon atmosphere and utilizing a graphite furnace to avoid material oxidation while remaining under the martials melting temperature are all examples of generating an adequate sintering environment for the materials at hand [33]. In addition to ensuring that the sintering environment is appropriate for the material at

hand, a profile determining time and temperature for sintering must also be developed. There are two classes of sintering profiles, 1 and 2 stage, that adhere to similar patterns of heating to a specific temperature time dependent upon a ramping rate (rate at which furnace reaches temperature), then soaking at this specific temperature for a specified amount of time. In 2 stage profiles this process occurs twice, then, once complete, the furnace can either be cooled naturally or at a cooling rate depending on the material. Another topic discussed in regards to the sintering process is shrinkage as a result of sintering. Shrinkage is a variable that relies on the material properties of the component and occurs at a specific temperature during the sintering process. It is believed that during sintering, as the free surface energy of a component decreases, particles within the component conjoin and assume a tighter, more compact structure, pointing to the surface tension as the motivation behind any shrinkage without the application of external stress [34]. When it comes to sintering ceramic components, a trend in research reveals high purity powders undergo sintering at lower temperatures and even shorter times than most other materials [35]. The reason being, additives such as low melting point oxides are implemented to high purity powder and have little effect on parameters such as piezoelectricity and mechanical properties while conserving energy and reducing of harmful emissions throughout sintering [36]. Recently, piezoelectric ceramics such as PZT have acquired interest due to their mechanical and piezoelectric properties with researchers conducting studies including analysis of effect of co-doping powders with cations to enhance piezoelectric properties [37]. The key variable in these studies however, relies on the sintering temperature during post fabrication, and the correlation between this temperature and both mechanical and piezoelectric properties of the component. It can be said that the sintering temperature of components affects facets of the microstructure such as porosity and grain size which determines the magnitude of the dielectric and piezoelectric constants. The optimization of piezoelectric properties within piezoceramic components can be achieved through the manipulation of the sintering temperature which can influence the porosity and pore morphology within a component [38]. The proper sintering technique for achieving fully dense piezoceramics without sacrificing some parameters whether it be mechanical or piezoelectric

properties has not yet been solved for, however studies have been successful in achieving a density high enough for some applications and in some cases optimizing piezoelectric and ferroelectric properties in ceramic components [39], [40]. 90% of all ceramics with enhanced properties are implemented toward electronic application with uses in devices such as capacitors and actuators that are beneficial for energy conservation, proving that perfecting the densification of ceramic materials through sintering is a pressing matter of research [41].

2.5 Piezoelectric materials

The term piezoelectricity is derived from the Greek word piezo which translates to pressure, correlating to the implied definition of pressurized electricity coined by Pierre and Jacques Curie in 1880 when a quartz material generated an electrical charge under pressure [42]. This discovery is known as the direct piezoelectric effect and has revolutionized methods of energy production since its application in World War 2. The reason why piezoelectric materials have maintained interest is due to their electromechanical properties and ability to generate electricity from pressure application, providing opportunities in applications such as vibration measurement, health monitoring, vibration based damage detection, and active vibration control [43]. Piezoelectric properties rely on the geometry and piezoelectric coefficients of the material which insinuate its capabilities based on capacitance and electromechanical coupling. The coupling withheld in a material provides the amount of mechanical energy available for conversion to electrical energy and the capacitance provides information on the loss in generation of electrical field that remains in the material [44]. Furthermore to maximize the energy output for a piezoelectric material, a low capacitance and high coupling coefficient provide the best parameters as coupling is proportional to piezoelectric coefficients and capacitance is dependent upon permittivity which when low, allows charges to yield more electric flux [45]. Researchers including Viswanath (*et al.* 2017) choose piezoelectric materials as the preferred method of vibration energy harvesting when compared to other techniques like electrostatic and electromagnetic methods, as piezoelectric materials have proven to yield higher energy densities

when applied to practical settings [46]. Similarly, in an effort by Todaro (*et al.* 2017) to develop and investigate performance of micro electric mechanical sensors (MEMS) utilizing epitaxial piezoelectric PZT thin films, a cantilever beam with a Si proof mass was subjected to a resonant frequency of 2.3 kHz. This material was selected due to excellent piezoelectric coefficients along with low dielectric constants and yielded a power of 13μW/g2, a current of 48μA/g, and a voltage of 0.27V/g as a product of the selected resonant frequency [47]. In addition to implementation of conventional piezoelectric materials towards energy harvesting devices, piezoelectric composites are also being employed to recover unused power from ambient environments. Piezoelectric fiber composites offer thin geometries, flexibility, and exceptional mechanical toughness that easily allow for integration into composite laminates [48]. Flexible PZT composites such as active fiber composite (AFC) and macro fiber composite (MFC) are used today in several energy conversion devices such as transducers and actuators as their flexibility and easy shaping allows for mechanical impedance matching, a useful tool in energy harvesting. Regardless of their capabilities, researchers continue to work on improving the environmental friendliness of piezoelectric materials. The toxicity and lead content of widely used materials such as PZT become volatile at elevated temperatures and have even been subjected to legislation of the European Union to prohibit use of hazardous substances [49]. This prompted researchers to investigate alternative lead free piezoelectric materials such as bismuth sodium titanate and alkali niobates which do not possess the degree of piezoelectric potential of conventional materials like PZT, but still hold stable piezoelectric characteristics. The next development in terms of piezoelectric materials are sensors capable of monitoring structural health and conditions. These sensors can be applied in several industries including the aerospace industry and assist in extending the lifespan while reducing maintenance costs of traditional sensors. The key in the development of these sensors lies within utilizing a material with excellent piezoelectric properties that can also be susceptible to any damages that can be incurred in harsh environments presented by industry applications. In addition to power and weight requirements, piezoelectric materials must be able to withstand high temperatures (>150°C), high pressure (>.1 MPa), mechanical shock of

acceleration (>10g), radiation, corrosive environment, and aggressive atmospheres [50]. Currently researchers continue to pursue a material that is capable of meeting these requirements, however other work such as the packaging of these materials is being conducted to further assist in the development of a self-sufficient component in a harsh environment. Energy harvesting fulfills a wide range of applications, however it would not be possible without the implementation of piezoelectric materials as the primary source for ambient energy generation when subjected to dynamic energy [51]. Whether research focuses on development of safer materials, improvement of efficiency, or characterization for industrial application, the information obtained regarding these materials provide a basis for future researcher to build upon for a brighter future.

2.6 Thermal energy harvesting

Recently, fully autonomous sensor networks are of great interest as demands for electronics with longer lifespans continuously increase, calling for a solution such as thermal energy harvesting as the conversion from ambient thermal energy to electrical energy is essentially an everlasting method of powering these sensors [52]. Since 2002, 50% of energy consumed in the United States was unaccounted for as waste heat dissipated to the environment by means of heat pumps, refrigeration, and power [53], [54]. As a part of the push to develop autonomous electronics capable of self-sustainability in harsh environments, researchers aim to recycle thermal energy normally dissipated into the environment, to continuously restore energy expended in these systems [55]. This is accomplished through thermal energy harvesting, which occurs by the pyroelectric effect in temperature variations or via the Seebeck effect when a temperature gradient is present. While a beneficial tool for energy harvesting, temperature gradients typically coincide with thermoelectric materials, which is not a point of emphasis for the research conducted in this work due to the inefficiency of the irreversible thermodynamic process. With that in mind, the pyroelectric effect is a property of dielectric materials such as PZT, that respond to temperature variations with spontaneous electrical polarization in the form of a current from the induced charge

due to its polar point symmetry [56]. This current described can be formulated into **Error! Reference source not found.** [57],

Equation 1 $$i_p = Ap\frac{dT}{dt}$$

where ip denotes the current generated spontaneously as a result of the change of temperatures, A denotes the surface area of the electrode, p denotes the pyroelectric coefficient of the material, and dT/dt denotes the rate at which the temperatures change. Pyroelectricity can further be understood as the behavior of the surface charge of a component when the ambient temperature is subjected to change, whether it be heated and dipoles become disoriented, or cooled and dipoles regain original orientation [58]. The heating conditions lead to a loss of free charges that are able to move across the surface of the component, whereas cooling conditions perform the opposite function. Material properties are the key component in this conversion from thermal to electric energy and determine both efficiency and power output that piezoelectric articles comprised of these materials yield. Cuadras (*et al.* 2010) explores the thermal energy harvesting capabilities of PZT and PVDF films characterized as power sources through application of cyclical heating and cooling fluctuations to generate currents and harvest the charges in a capacitor. From this investigation, it was confirmed that the current generated as a result of temperature fluctuations accumulated enough charge to power an autonomous sensor node and while both PZT and PVDF serve as adequate sources of benign energy, because of a greater pyroelectric coefficient, PZT produced a larger current [59].Temperature variations were induced through wind in the aforementioned experiment, however thermal energy is attainable from various sources such as solar energy [60], infrared energy [61], and even wearable technology [62]. With all of the available methods of obtaining this energy that would otherwise be dissipated and unused, it is difficult to avoid the potential of this unique method of powering electronic devices. As the culture of modern electronics continues to shift toward a demand for longer lifespans and decreased size of power

sources [63], thermal energy harvesting shows great promise as a ubiquitous energy source that can eliminate the use of batteries not only in areas of limited accessibility, but perhaps altogether, providing an alternative, cleaner and cost effective method of power generation.

2.7 Mechanical energy harvesting

Dating back to windmills utilized in 500-900 A.D., powering devices from environmentally benign sources through harvested energy has been an area of interest that has recently garnered popularity with the global demand for portable electronics [64]. The basis of this principle is to obtain electrical energy for harvesting by means of extracting energy generated from an operational environment. This is where the term, mechanical energy harvesting, can provide a solution for meeting these demands. Mechanical energy harvesting is a technique where it is possible to store and convert mechanical energy to electrical energy induced by mechanical strain via the piezoelectric effect [65]. The high energy densities of piezoelectric materials provide the most viable energy production solution when compared to other methods for harvesting energy. Furthermore, piezoelectric materials can be easily incorporated into systems subjected to dynamic energy, essentially presenting any vibrating host the possibility of harvesting mechanical energy [66]. When a piezoelectric material is subjected to any form of strain, an electrical voltage is produced and available for harvesting. The behavior of these piezoelectrics can be described mechanically and electrically by standard piezoelectric constitutive law in strain charge form [67] [68],

Equation 2 $$S = s^E T + dE$$

Equation 3 $$D = dT + \varepsilon^T E$$

where S indicates material strain tensors, T indicates material stress tensors induced electrically and mechanically, D represents charge density displacement, E represents electric field vectors, d represents a matrix of piezoelectric strain coefficients, SE represents an elastic compliance matrix, and ƐT represents a matrix of permittivity at constant stress. These constitutive equations provide

a representation of the materials abilities to generate a charge in response to mechanical stress, or the piezoelectric effect [69]. The key difference between piezoelectric materials and traditional sources of power is the internal impedance not being inductive, but capacitive, meaning that mechanical motion is able to produce a power output of different variations depending on the amplitude of the motion [70]. Examples of piezoelectric materials that have been successful subjects of mechanical to electrical energy conversion include zinc oxide (ZnO), PZT, cadmium sulfide (CdS), BTO, and gallium nitride (GaN) [71]. In an effort to maximize the power output harvested mechanically from piezoelectric materials, Lesieutre (*et al*. 2004) and others developed an adaptively controlled switching DC–DC converter. By switching to a converter for harnessing mechanical energy as opposed to traditional rectifying circuits, the power delivered to the energy storage unit was increased by 400% [72]. In a separate experiment conducted by Sodano (*et al.* 2004), an attempt to convert the ambient vibration energy from PZT material to electrical energy through the vibration of a cantilever beam equipped with several evenly distributed PZT patches was carried out. From this energy harvesting model, the output current produced by vibrations reached a maximum of .345 mA when measured across a 100Ω resistor at 30 Hz [73]. This is substantial as the energy produced can be harvested and used to power small devices such as actuators and sensors at any given time [74], essentially providing an endless energy supply to small electronics constantly subjected to mechanical stress or strain. Mechanical energy harvesting has received the most attention in comparison to other methods of harvesting benign energy, and although in some cases it is a technology that has been successfully implemented in several industries, it is not yet ready for commercialization. With continuing research, an optimum model for this energy harvesting technique will soon be discovered and will assist in the ongoing pursuit for cleaner energy.

2.8 Combined energy harvesting

Recently North American culture has developed a dependence on abundant, low cost fossil fuels, while ignoring the harmful environmental effects their use entails. Organizations such as the

US Department of Energy (DOE) actively research sources of low cost [75], ubiquitous energy as an alternative to these fossil fuels and have stumbled across the concept of combined energy harvesting. The term combined energy harvesting can be described as a process where benign ambient waste energy is attainable and harvested from a multitude of sources such as thermal, solar, or vibration energy [76], [77], [78], [79]. This energy is stored in a source such as a capacitor then converted to electrical energy. In the above sections, the individual successes of thermal and mechanical energy harvesting through piezoelectric and pyroelectric materials can be observed, however an important detail regarding pyroelectric materials, is that they are also piezoelectric by nature. What this means is that in addition to the charge generated through temperature fluctuations, the piezoelectric nature of pyroelectric materials can assist in the production of electrical power through mechanical strain [80]. Provided the appropriate material and method of storage is utilized, it is possible to simultaneously harvest a variety of ambient energy sources. In an effort to confirm this statement, a recent study conducted by Bandyopadhyay (*et al.* 2012) tested the capability of a single inductor to simultaneously harvest photovalic, thermoelectric, and piezoelectric energies. In the study a multi input/output switch matrix is employed to extract maximum power from individual energy harvesting sources. By implementing this architecture design energy harvesting efficiency boosts of 83% (photovalic energy), 58% (thermoelectric energy), and 79% (piezoelectric energy) were achieved and processed simultaneously through one inductor [81]. This confirms that energies harvested from several sources can be simultaneously harvested into one mechanism for conversion to electrical energy, however further research must be conducted for the concept to become commercialized. Though not much research has been conducted on the subject, combined energy harvesting has potential to improve efficiencies of traditional energy harvesting practices and can multiply electrical energy output varying on the amount of ambient energy sources available. For these reasons, combined energy harvesting is a ubiquitous alternative source of energy juxtapose to fossil fuels that produce harmful CO_2 emissions.

Chapter 3: Materials & methods

3.1 Piezoelectric materials

For the BJ AM process, each variation of material utilized for component fabrication was in powder form for compatibility with the ExOne M-lab BJ printing system (ExOne, North Huntingdon, PA). The manufacturer information and material properties for materials used in this work including $LiNbO_3$, BTO, PZT, PZT-5A, and GO are reported in in Table 2, Table 3, Table 4, Table 5, and Table 6 respectively. The solid PZT-5A sample was purchased from Piezo Systems Inc. (Piezo Systems Inc., Woburn, MA) and the aqueous GO solution used to enhance the piezoelectric properties of the AM fabricated piezoelectric materials was purchased from Goographene (Goographene, Merrifield, VA). These materials were altered to enhance material properties for comparison of mechanical and piezoelectric properties amongst fabricated component variations.

Table 2 Material properties of $LiNbO_3$ powder.

Material properties	
Name	Lithium niobate
Supplier	American Elements
Particle size (µm)	8
Pyroelectric Coefficient ($C/K \cdot m^2$)	-8.3×10^{-5}
Curie Temperature (°C)	1133 ± 3
Melting Point (°C)	1253
Density (g/cm^3)	4.647
Heat Capacity (J/K·mol)	89
Capacitance (F)	2.319×10^{-9}
Resistance (Ω)	9.349×10^{5}
Crystal structure	Trigonal

Table 3 Material properties of BTO powder.

Material properties	
Name	Barium titanate
Supplier	Goodfellow USA
Particle size (µm)	45
Piezoelectric coefficient [g33] (V-m/N)	22×10^{-3}
Curie temperature (°C)	$123 \pm .6$
Melting point (°C)	1625
Density (g/cm^3)	6.02
Dielectric constant	2000
Crystal structure	Perovskite

Table 4 Material properties of PZT powder.

Material properties	
Name	Lead zirconate titanate
Supplier	American Piezo Corporation
Particle size (µm)	150
Piezoelectric coefficient [g33] (V-m/N)	25×10^{-3}
Curie Temperature (°C)	350
Melting Point (°C)	1350
Density (g/cm^3)	7.6
Dielectric constant	3000
Heat Capacity (J/K·mol)	89
Crystal structure	Perovskite

Table 5 Material properties of PZT-5A sample.

Sample properties	
Name	Lead-Zirconate Titanate 5A
Supplier	Piezo Systems Inc.
Area (mm^2)	2500
Thickness (mm)	1.0
Piezoelectric Coefficient [g_{33}] (V-m/N)	25×10^{-3}
Curie Temperature (°C)	350
Density (g/cm^3)	7.8
Heat Capacity (J/K·mol)	89
Capacitance (F)	4.040×10^{-8}
Resistance (Ω)	1.826×10^{5}

Table 6 Material properties of GO aqueous solution.

Material properties	
Name	Graphene oxide
Supplier	Goographene
Theoretical specific surface area (m^2g^{-1})	2630
Electron mobility ($cm^2V^{-1}s^{-1}$)	200000
Optical transmittance (%)	97.7
Melting Point (°C)	3600
Density (g/cm^3)	0.5
Heat Capacity (J/K·mol)	89
Thermal conductivity ($Wm^{-1}k^{-1}$)	5000
Young's modulus (TPa)	1.0

3.2 Binder preparation

The binder solution (BS004 Solvent Binder 04) purchased from ExOne was solvent based and intended for direct metal printing. In an effort to further enhance the piezoelectric properties of fabricated ceramic components, the binder solution was doped with variations of weight concentrations of the aqueous GO solution. The single layered GO solution was purchased from Goographene and was prepared by dissolving 5 milligrams of graphene per 1 milliliter of distilled water by means of ultrasonic vibration. Due to the presence of oxygen functional groups within GO, easy dispersion in organic solvents such as the binder was an advantageous quality of the material. Particle dispersion can improve electrical and mechanical properties in ceramic and polymer matrix materials. The doping process was performed at weight percentages of 5%, 10%, 15%, 20%, 25% and 30% of the aqueous GO solution in relation to 30 milliliters of binder solution to formulate the binder-GO mixtures. The purpose of adding several weight concentrations of aqueous graphene solution to binder solution was to first determine the surface tension of each concentration, then determine the concentration that provided the highest dielectric constant in a fabricated ceramic component. Once both solutions were combined in the same vile, they were transported to a vortex mixer which rotated for a duration of 5 minutes until the contents were mixed and the graphene particles were dispersed throughout the mixture.

3.3 Binder characterization

The next portion of the binder characterization process was to determine the angle of contact between a surface and liquid which determined the wettability of the mixtures. If any iteration of the solution exhibited bad results in terms of wettability, it would not be possible to fabricate components utilizing this concentration in an AM system moving forward. ASTM standard D733 indicated that angles above 90° are classified as hydrophobic and would repel against the surface, whereas angles below 45° show excellent wettability [82]. The contact angles of water were used as a starting test reference to compare with the contact angles obtained from the binder-graphene mixtures. Not only did water serve as an excellent reference point for comparison of test angles, but it also served as an agent of estimating surface cleanliness before and between tests. The testing setup used to determine the contact angle included a makeshift goniometer scale, which was recommended by the aforementioned ASTM standard. The test setup called for an environment at a room temperature of 23°C and a humidity less than 50%. An adjustable platform would be used as the stage of the goniometer and a high quality camera would be set level to the surface of the stage and held in place with clamping mechanisms. In order to achieve adequate drop placement and formation, a pipet was used to disperse each test drop, no greater than 20μL of fluid, upon the platform. The tip of the pipet was placed at an estimated 3mm from the surface of the platform and the droplet was then dispensed. A drop of each mixture was individually placed on the surface of the goniometer scale and a high quality image of each drop was captured. The images of each drop were taken quickly, as time lapses lead to changes in the angle of the drop. In addition to this, a drop of water and pure binder solution were measured for reference purposes. Once an image of each droplet had been captured and processed, the angle of contact was taken with the aid of a protractor software.

3.4 Powder mixing

3.4.1 $LiNbO_3$ & GO

$LiNbO_3$ mixed with GO was the first iteration of powder enhancement that took place for the research. As opposed to doping binder and jetting it through a print head during the AM process, the $LiNbO_3$ powder was mixed and dried with the aqueous GO solution prior to printing. 150 grams of $LiNbO_3$ powder purchased from Goodfellow USA were carefully spooned into a pestle and mortar setup. Since the GO solution only possessed 5 mg of graphene per 1 ml of distilled water, 750 ml of the aqueous solution was used within the mixture to equal 1% GO of the total weight. If 750 ml of this solution was directly added in its entirety to the powder, it would be disproportionate and the mixture would maintain the aqueous qualities possessed by the GO solution. To avoid this and obtain a miry consistency from implementing high amounts of GO solution to the mixture, increments of 50 ml of GO solution were added to the powder. Once the solution was added to the powder, the contents were mixed with a plastic spoon and placed into a curing oven for 2 hours at a temperature of 150°C to expedite the drying process. Once dried, more GO solution was added to the powder mixture and the process was repeated until a total of 750 ml of the GO solution was added. After the powder mixing process was completed, the powder was removed of any inconsistencies in the form of dried agglomerates by manually breaking them down with the pestle instrument and further prepared for printing. The BJ-fabricated components possessed dimensions of 3mm thickness and 27mm diameter to replicate the dimensions of the pellet samples.

3.4.2 BTO & $LiNbO_3$

Through experimentation it was observed that pure $LiNbO_3$ did not have the desired spreadability and flowability for BJ. Therefore, BTO and $LiNbO_3$ were mixed to improve both characteristics. Flowability is the degree of ease that a powder is able to flow under specified conditions as described in ASTM standard B213 [83]. As opposed to spherical particles, the $LiNbO_3$ particles were irregularly shaped and formed agglomerates indicating limited flowability.

The flowability was quantified with a Hall Flow Meter test, which required the use of a Hall Flow Meter, comprised of a workbench supporting the powder flowmeter stand and a funnel equipped with an orifice of 2.54mm in diameter for measurement of the powder flow rate. In this standard test, 50 grams of the respective powder was weighed and poured into the funnel mechanism then timed until the funnel was emptied. For the experimental analysis performed, a total of three trials were performed and recorded. Using the three recorded times, the average time for powder flowability was calculated, however in the case of pure $LiNbO_3$ there was no mobility of powder through the orifice. The lack of flowability led to the addition of BTO, a powder spherical in shape and previously successfully spread with the BJ printing process [30]. In this mixing process, a scale was used to weigh 75 grams of BTO and 50 grams of $LiNbO_3$ prior to placing the powders into the same container. Once in the same container, the mixture was then transported to an Inversina 2L three dimensional inversion kinematics tumbler mixer (Bioengineering Inc., Somerville, MA). The powder mixture was placed into a sealed stainless steel container equipped with an O-ring to prevent powder leakage. Once this container was sealed, the safety hood of the tumbler (see Figure 4) was opened and the metal container was then placed into a mixing basket that was fixated into the instrumentation with a rubber fixation ring. The mixing basket was finally secured within the tumbler via a tightened rubber tension ring. Speed and time were determined from a power knob located directly on the instrumentation. For most mixtures used within this system, a time of one hour provided the desired distribution of particle size in a single batch. Once this mixture was obtained, it was ready for use within a BJ printing process.

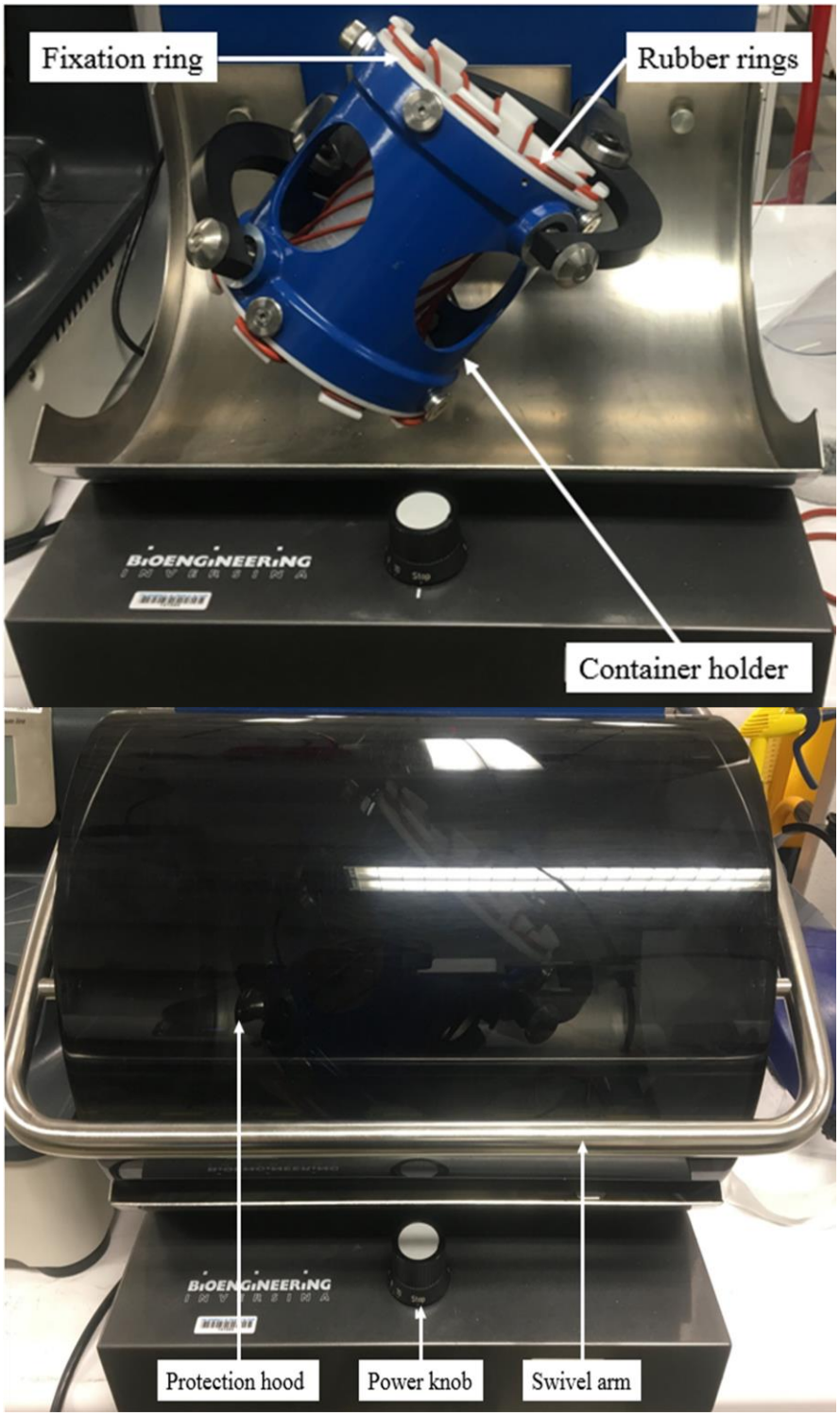

Figure 4 Inversina 2L powder mixing mechanism.

3.4.3 PZT & BTO

PZT and BTO were combined on the premise that layer size reduction was not possible solely through the use of pure PZT in a BJ AM procedure. The reason why layer size reduction was of such importance was because as layer size reduced, so did porosity leading to higher part density. The large particle size of pure PZT did not allow the roller component of the ExOne system to spread small layers of powder across the powder bed, thus leading to the theory that if these larger particles were mixed with the smaller particles of BTO, a reduction in layer size was possible. This mixture was accomplished by using a scale to weigh out a 50:50 ratio of both powders and placing them in the same container. The powder mixture was mixed for one hour using the Inversina 2L tumbler. Ball milling was not required beyond this point as an altered particle size distribution was desired. Visual representation of this powder mixing instrumentation can be observed in Figure 4**Error! Reference source not found.**. Once this mixture of powders was acquired, it was ready to be used in the ExOne system for the BJ process to be carried out.

3.5 Pellet sample fabrication

Once it was confirmed that each variance of binder-graphene mixtures displayed similar wettability characteristics when compared to unenhanced binder to the surface, the binding effect was quantified through the fabrication of circular pellet samples comprised of each aforementioned concentrations of binder mixture and powder material. In addition to quantifying the binding effect, pellet samples were fabricated as a preliminary step towards additively manufacturing ceramic components for combined energy harvesting testing. Ultimately, these pellet samples were subjected to dielectric testing to determine which range of doped binder would produce the highest dielectric constant from the material. Initially BTO was chosen for these preliminary studies because of its piezoelectric characteristics and lower cost in comparison to similar materials. In order to fabricate these pellet samples, a ceramic paste comprised of powder material (pure or enhanced) and binder solution (varying concentrations of GO) was mixed with a pestle and mortar.

Each sample called for 15 grams of powder and 6 drops of binder solution to closely simulate the amounts of powder and binders used in a BJ AM process. Once the constituents of the paste were adequately mixed, the paste was placed into a casting mold for pellet fabrication. Using a hydraulic press, a compressive force of 3000 N was applied to the mold and held for a total of two minutes, relinquishing the sample of all excess binder and compacting each component of the mixture to form a green body. This applied force prevented any possible breakage to the green body and allowed for easily handling once it was removed from the casting. Two samples of each iteration of binder concentration, 25mm in diameter and 5mm thickness were fabricated from this process. Once the green body samples were removed from the pellet mold they were then subjected to curing (two hours at 200°C followed by natural cooling) which allowed components to strengthen through crosslinking, once again simulating the BJ AM process. Once cured, half of the samples underwent a sintering process where a binder burnout at a temperature of 600°C for 20 minutes, a soak at 1200°C for 2 hours, and a ramping rate of 10°C/min to reach all holds within the profile was executed followed by a natural cooling process to avoid temperature shock. The other half of the fabricated samples only went as far as the curing process meaning that the two sets of samples were available for preparation for dielectric testing. Silver paint (SP-60+ Water Based Silver Ink) purchased from M.E. Taylor Engineering Inc. was applied to the top and bottom surfaces of each sample via brushing. This silver paint consisted of silver, a viscous polymer, and solvent to allow brushing upon non-conductive surfaces. To ensure that the paint adhered to the sample upon application to one surface, each sample was placed into an oven for 25 minutes at a temperature of 150°C. Furthermore, this drying process assisted in evaporating polymers and solvents existing within the mixture to leave behind a conductive silver surface residing on the painted component. Once the silver paint dried, copper tape was applied to the top and bottom surfaces of the samples, acting as extensions of the component to allow positive and negative clamps connected to electrical test instrumentation to be attached. The test equipment used was an LCR meter which was capable of measuring the capacitance, inductance, and resistance of electrical components. In this case the

LCR meter was used to measure the capacitance of the pellet samples. Capacitance was quantified by the equation,

Equation 4 $$C_p = \varepsilon_o \varepsilon_r \frac{A}{t}$$

where C_p represented the capacitance obtained, ε_o represented the permittivity of air, ε_r represented the dielectric constant of the sample, A represented the cross sectional area of the sample, and t represented the thickness of the sample. Since the dielectric constant was the only unknown in the equation following the measurement of the capacitance from the LCR meter, it was solved simply by rearranging the equation to,

Equation 5 $$\varepsilon_r = \frac{C_p * t}{\varepsilon_o * A}$$

Once obtained, the dielectric properties were compared to one another in order to determine which concentration of graphene mixed with binder solution would produce the highest piezoelectric characteristics in an AM process.

3.6 Piezoelectric measurement

The d33 property of samples containing PZT was measured to determine the degree of piezoelectricity that these samples withheld. Using a YE2730A d33 meter (Sinocera Piezotronics Inc., Yangzhou City, Jiangsu Province, P.R. China) the d33 value would be obtained by first thermally poling samples. This poling process was a technique utilized to relax the material for dipole movement within the component. Furthermore, this dipole movement arranged positive and negative charges to their own respective ends of the component in conjunction with one another. To begin this poling process, the sample was clamped to an electrical cable and placed into silicon oil as it was a non-conductive solution. Once submerged, the oil was heated to 120°C for two hours to relax the material. Then a voltage was applied through the cable at a current of 10μA to electrically poll the sample. A Static electric field of 1.2Kv/mm was utilized for all PZT samples.

Once this process was completed the sample was placed between the two probes of the aforementioned d33 meter. Once secure, the d33 meter was switched on and a d33 reading of one surface of the component was measured as a response to the light pressure applied by the probes. This reading was either positive or negative as the dipoles shifted all positive or negative on one side of the component. To ensure that the reading was accurate, the component was flipped and secured again. The flipped reading would resemble the previous reading (98%-100%), however it would possess the opposite positive or negative sign. Visual representation of this poling process as well as the YE2730A d33 meter can be observed in Figure 5 and Figure 6.

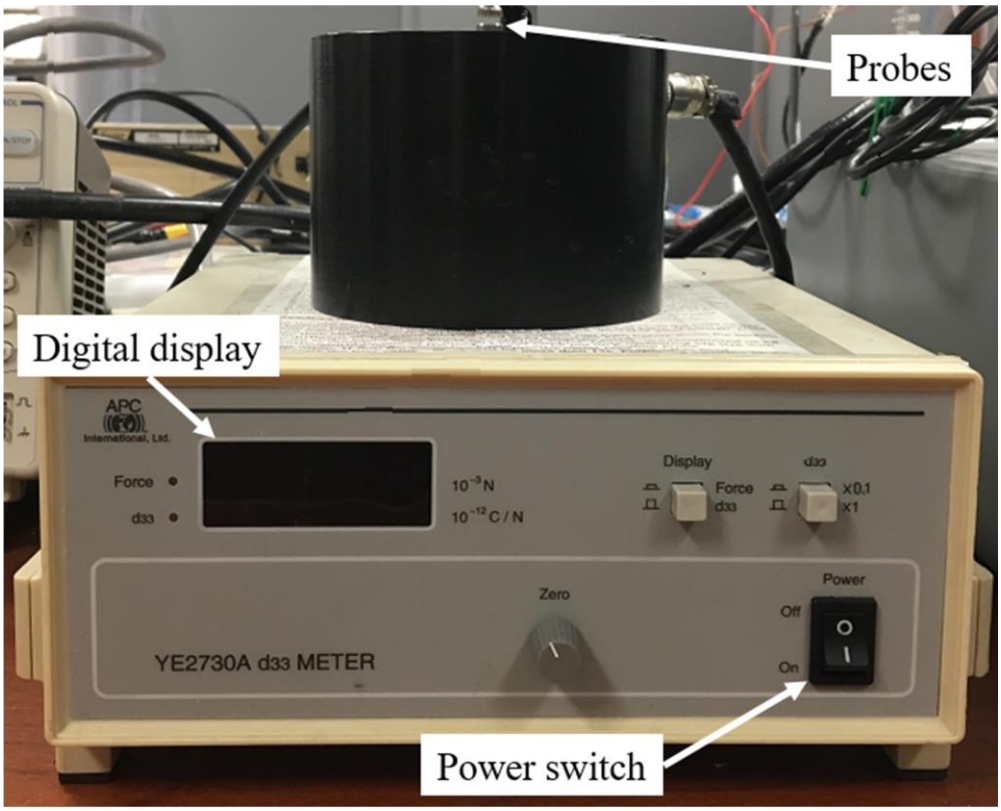

Figure 5 YE2730A d33 meter used for determining piezoelectricity of samples.

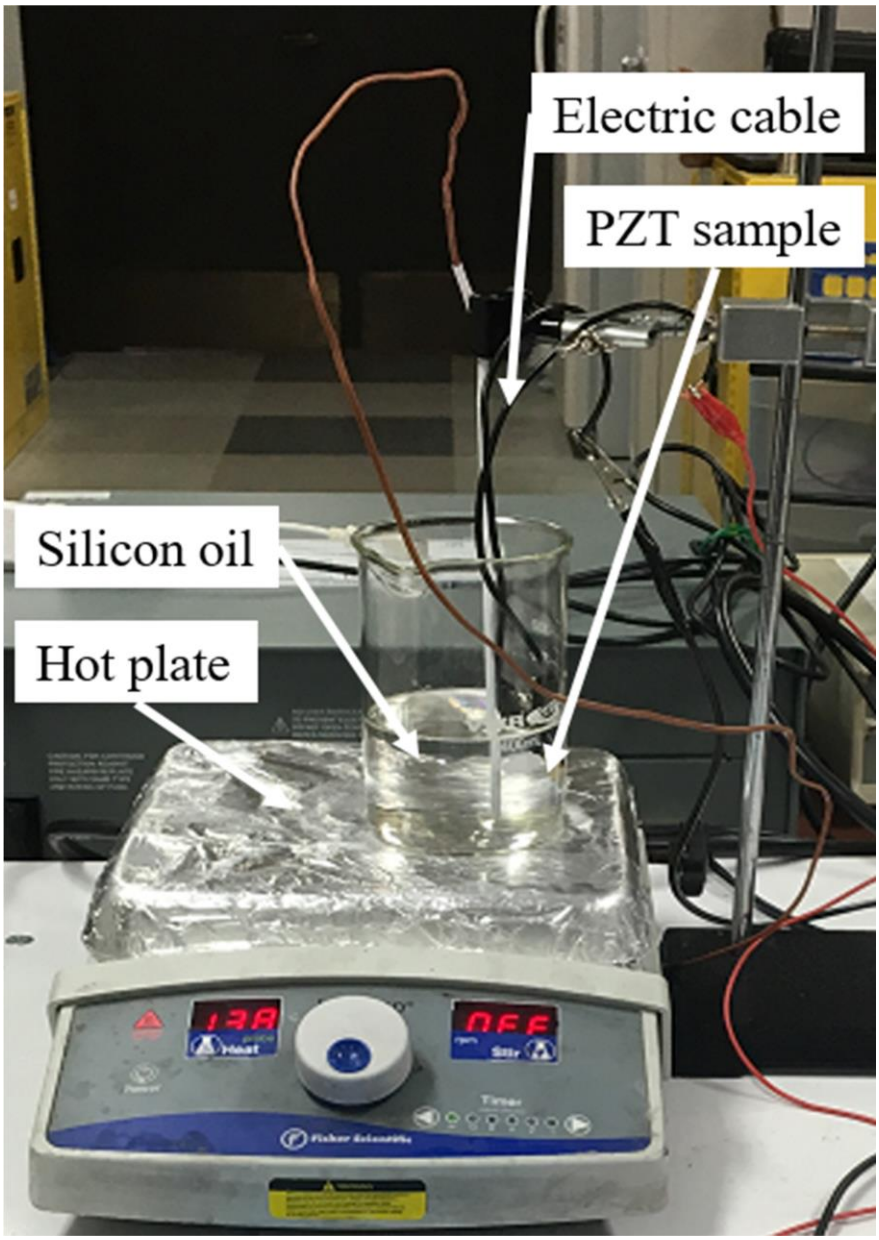

Figure 6 Thermal poling setup for PZT samples.

3.7 Additive manufacturing of piezoelectric materials

3.7.1 Starting new materials

In this material development research BTO, $LiNbO_3$, PZT, BTO & $LiNbO_3$ mixture, $LiNbO_3$ & GO mixture, and PZT & BTO mixture were investigated. For each new material or material swap, the ExOne M-Lab BJ printer was cleaned thoroughly to avoid powder

contamination. The powder packing rate (PPR) was configured next. In order to accomplish this, a feeding ratio coinciding with the powder particle size was selected and 100 layers of powder was spread from the feed bed onto the build platform. Once 100 layers were spread onto the build platform, the weight of the 100 layers was measured and the volume of this powder was determined from the following equation,

Equation 6 $$V = \frac{W_p}{(l * w) * l_t}$$

where V represented the volume of the 100 layer sample, W_P represented the weight of the 100 layers spread upon the build platform, l represented the length of the build platform, w represented the width of the build platform, and l_t represented the layer thickness of each layer of powder spread. With the volume of the powder in hand, this value was used to find the PPR for the new material using the following equation,

Equation 7 $$PPR = \left(\frac{V}{\rho_{material}}\right) * 100$$

where the PPR was found using the volume of the 100 layers of powder denoted by V and the density of the material denoted by $\rho_{material}$ then multiplied by 100 to obtain a percentage. For mixtures of materials, the PPR for each individual material was obtained then averaged out.

3.7.2 Saturation test

In order to ensure that there were no missing jets on the print head, a test pattern was printed upon a cardboard substrate. The test pattern revealed missing areas where binder was not being dispensed from the printhead which were later identified and accounted for. In order to bypass the issue of missing jets, multiple “prime”, “prime & fire”, and “wipe print head” commands were also executed. From this step, a saturation test was performed to ensure that enough binder was being dispensed from the print head. This was completed by measuring the drop volume from the print head for a total of five times and obtaining the average from these drop volume trials. The drop volume was measured by dispensing 10,000 droplets of binder upon a cloth substrate located

in the gutter of the printer. The difference of weight in the cloth before and after the droplets were dispensed was recorded and used as one of the five variables in the drop volume test. This average allowed the M-Lab system to compute a saturation for a given print job.

3.7.3 Powder set up

A build platform was placed upon the Z axis platform which was then lowered 4mm to compensate for the foundation layers of powder that were spread upon it. The F axis, which is also known as the feed bed due to the powder supply residing on this axis, was lowered to its bottom positon and powder was placed into the empty area. From here, a level spread task was executed, spreading the powder across both platforms until completely leveled and smoothed. Once the level spread was used to set up the powder, 3-5 executions of a normal spread task were performed to create the foundation layers of the component being manufactured. This type of spread raised the F axis up one layer and spread it across the Z axis platform which did not move, thus creating a smooth foundation layer. Next a part was selected for fabrication. Once an STL file within the user interface was selected, it was then placed on a simulated build platform in a desired orientation. Once selected, the user was able to adjust material-specific processing parameters. Once this was completed, a few checks were executed: ensuring the binder and cleaner receptacles were full, the waste receptacle was empty, and the heating power was at 60%. The print was then commenced.

3.8 Additive manufacturing process parameters

Printing parameters varied amongst materials and were sometimes found in prior research, however when materials were altered, new parameters needed to be developed. In the case of most ceramics utilized for manufacturing components via the ExOne M-Lab, a large layer size allowed for adequate spreadability from the feed bed onto the build platform. Of course, this large layer size was associated with low mechanical strength in materials so in addition to adjusting this layer size, parameters that greatly influenced mechanical strength such as binder saturation, feed ratio, and spread speed varied amongst materials [17]. In the case of a PZT & BTO powder mixture iteration, due to the larger particle size distribution in batches, a smaller feed ratio was utilized for

component fabrication. Furthermore, a saturation percentage of 200 was utilized to compensate for the large layer size. This high saturation percentage allowed for the solvent based binder solution to penetrate each layer of powder, thus allowing for proper adhesion. These parameters, along with others for this powder mixture can be observed in **Error! Reference source not found.**. In the case of $LiNbO_3$ & GO, parameters varied in comparison to the PZT mixtures based upon the smaller particle size of $LiNbO_3$. Difficulties in spreadability for this iteration were overcome by utilizing the minimum spread speed available (5 mm/s) and the maximum saturation percentage (300%). These parameters were also implemented to bypass possible low mechanical strength from printed components. In addition to this, a maximum feed ratio (1.90) was utilized to spread the small particles from the feed bed onto the build platform. Parameters for this iteration are displayed in **Error! Reference source not found.**. Finally, printing parameters for a mixture of $LiNbO_3$ & BTO can be observed in **Error! Reference source not found.**. Due to the small particle size of $LiNbO_3$, the maximum feed ratio and spread speed were maintained from the $LiNbO_3$ & GO mixture. These parameters allowed for the best possible outcomes in terms of AM. Further into this investigation, mechanical properties such as density of the components fabricated from these parameters were determined.

Table 7 PZT & BTO BJ processing parameters

BJ processing parameters (PZT & BTO)	
Part file processing	
Layer thickness (μm)	150
X, Y, Z default STL scale factor	1.0
Saturation & waveform	
Y print speed (mm/sec)	150
Y drop spacing (μm)	29.788
Powder packing rate (%)	58.480
Desired saturation (%)	200
Print passes per X jet spacing	18
Computed X drop spacing (μm)	28.222
Binder density (g/ml)	0.990
Computed droplet frequency (Hz)	5036
Spreading & drying	
Initial spread speed (mm/sec)	20
Drying time (sec)	120
Spreader rapid traverse speed (mm/sec)	35
Left/right spreader rapid traverse border (mm)	5
Feed powder to layer thickness ratio	1.75
Build/feed retract distance (mm)	0.5
Initialization & cleaning	
Foundation layers	2
Foundation powder to layer thickness ratio	2

Table 8 $LiNbO_3$ & GO BJ processing parameters

BJ processing parameters ($LiNbO_3$ & GO)	
Part file processing	
Layer thickness (μm)	120
X, Y, Z default STL scale factor	1.0
Saturation & waveform	
Y print speed (mm/sec)	150
Y drop spacing (μm)	27.187
Powder packing rate (%)	62.090
Desired saturation (%)	300
Print passes per X jet spacing	18
Computed X drop spacing (μm)	28.222
Binder density (g/ml)	0.990
Computed droplet frequency (Hz)	5517
Spreading & drying	
Initial spread speed (mm/sec)	5
Drying time (sec)	90
Spreader rapid traverse speed (mm/sec)	5
Left/right spreader rapid traverse border (mm)	5
Feed powder to layer thickness ratio	1.90
Build/feed retract distance (mm)	0.5
Initialization & cleaning	
Foundation layers	2
Foundation powder to layer thickness ratio	2

Table 9 $LiNbO_3$ & BTO BJ processing parameters

BJ processing parameters ($LiNbO_3$ & BTO)	
Part file processing	
Layer thickness (µm)	120
X, Y, Z default STL scale factor	1.0
Saturation & waveform	
Y print speed (mm/sec)	150
Y drop spacing (µm)	33.218
Powder packing rate (%)	63.680
Desired saturation (%)	200
Print passes per X jet spacing	16
Computed X drop spacing (µm)	31.750
Binder density (g/ml)	0.990
Computed droplet frequency (Hz)	4516
Spreading & drying	
Initial spread speed (mm/sec)	5
Drying time (sec)	90
Spreader rapid traverse speed (mm/sec)	5
Left/right spreader rapid traverse border (mm)	5
Feed powder to layer thickness ratio	1.90
Build/feed retract distance (mm)	0.5
Initialization & cleaning	
Foundation layers	2
Foundation powder to layer thickness ratio	2

3.9 Heat treatment of samples

As part of the BJ AM process, fabricated green body components were subjected to heat treatments to achieve higher density and obtain improved mechanical properties. Directly after the BJ process, green body components were transported to a curing oven for crosslinking polymers within the ethylene glycol monomethyl ether binder solution and powder particles. The curing oven provided by ExOne was pre heated to a temperature of 200°C. Green bodies were then placed into the curing oven for a total of 2 hours and were naturally cooled to avoid temperature shock. The cured binder acted as an adhesive, enhancing the mechanical properties of the component. After this process components were less susceptible to breakage from handling, providing the opportunity to remove excess powder. Once the de-powdering was completed, further heat treatment was performed to accomplish full density. Sintering components was the next step in

bringing samples closer to achieving increased density, however, unlike the curing process, sintering profiles varied between the materials. The sintering profiles of each material can be observed in Figure 7, Figure 8, and Figure 9. A similar pattern between all sintering processes was the rate at which they were ramped to holding areas (10°C/min) and a holding period at a temperature of 600°C. This holding period was used to burnout binder. In addition to this, all components were naturally cooled to avoid temperature shock. Components comprised of $LiNbO_3$ & GO were sintered in graphite crucibles under an inert argon environment to avoid oxidation of the GO existing within the samples. Components comprised of PZT & BTO were sintered in alumina crucibles and sealed with alumina paste. Before the crucibles were sealed, a bit of pure PZT powder was also placed into the crucible to prevent samples from oxidizing. The crucibles were sealed to prevent the release of volatile fumes due to the lead content existing within the material. Finally components comprised of BTO & $LiNbO_3$ were sintered in alumina crucibles with no inert environment, however adhering to the lower melting temperature of $LiNbO_3$. From this sintering process, density measurements of the components were recorded.

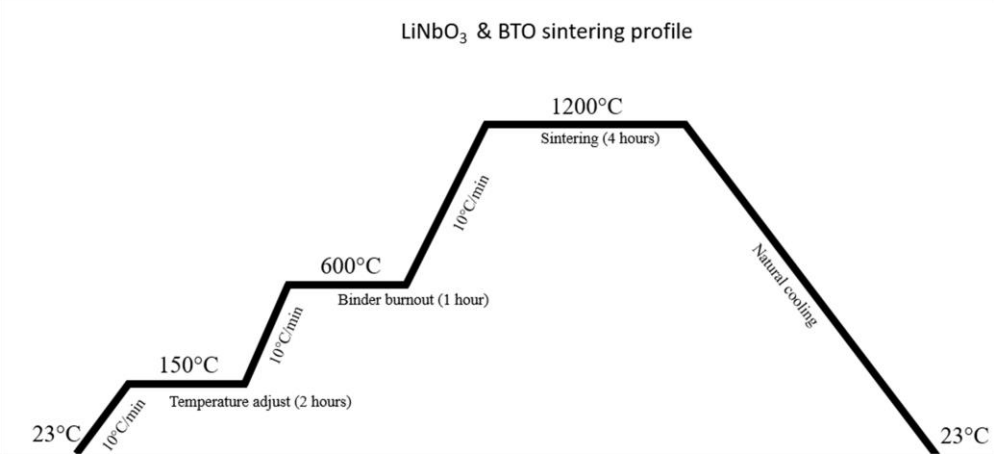

Figure 7 $LiNbO_3$ & BTO mixture sintering profile.

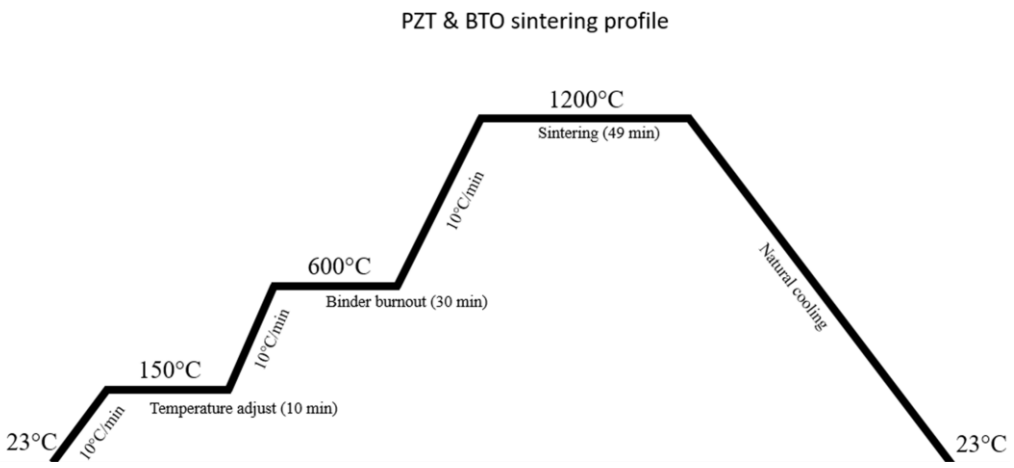

Figure 8 PZT & BTO mixture sintering profile.

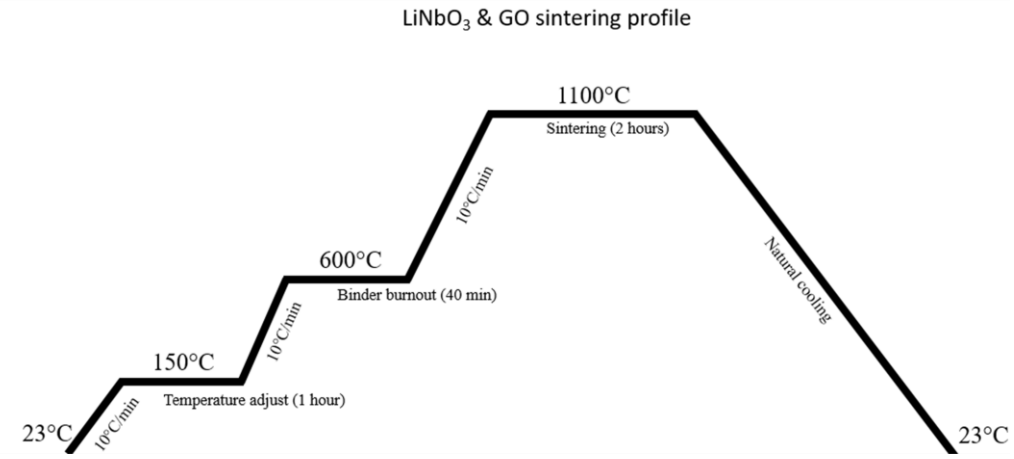

Figure 9 $LiNbO_3$ & GO mixture sintering profile.

3.10 Density measurements

Ultimately, a component capable of withstanding harsh environments was desired as it would be implemented within a sensor subjected to extreme conditions. A good indication of the toughness of a component resided within its density. Post fabrication density measurements were taken before and after sintering. These density values were obtained utilizing the following equation for the density of a cylinder, as all fabricated pellet components were cylindrical in shape,

Equation 8 $$\rho = \frac{m}{\pi * r^2 * h}$$

where m represented the mass of the sample in grams, r represented the radius of the circular sample in millimeters, and h represented the height of the sample in millimeters. These measurements were acquired through the aid of a caliper, where the diameter and height of the samples were measured and recorded. The mass of the sample was acquired by using a scale. Once the density of the sample was obtained, it was then subjected to an equation where it was divided by the theoretical density (TD) of the material obtained through a safety data sheet (SDS) provided by the manufacturer. This equation was implemented to obtain an indication of what percentage of full density the sample had achieved. This equation is represented as,

Equation 9 $$\rho_{percentage} = \frac{\rho}{\rho_{theoretical}}$$

where ρ was the density obtained from the fabricated sample and $\rho_{theoretical}$ represented the TD of the material, both in $\frac{g}{cm^3}$. Once obtained, this percentage revealed how close the component was to achieving full density and dictated both the strength and mechanical properties of the component. If the result of the acquired density was insufficient, process parameter manipulation was required to further densify the component.

3.11 Energy harvesting

3.11.1 Introduction

With the rapid development of self-sufficient devices in the field of energy harvesting, substantial research devoted to harvesting waste heat energy via the pyroelectric effect and waste vibrational energy via the piezoelectric effect has been conducted. Although individually these methods of harvesting benign energy have been well researched, no studies quantifying the energy produced from a single material through coupled excitation has been conducted. Since most piezoelectric materials naturally possess pyroelectric characteristics, it would be possible to subject a material to several variants of excitation in unison to simultaneously harvest the ambient

energies produced. In the early stages of combined energy harvesting experimentation, a composite material called PZT-5A known for exhibiting both piezoelectric and pyroelectric properties was purchased from a manufacturer and acted as a preliminary stepping stone toward a BJ fabricated component capable of withstanding stress variants to produce energy. In this experiment a 50 mm by 50 mm PZT-5A square plate sample with a thickness of 1mm was simultaneously subjected to thermal and mechanical stresses via a customized testing setup to be coupled as a thermal and mechanical energy harvesting device. Visual representation of the designed load frame fixture can be observed in Figure 10.Upon application of these stresses a custom rectifying circuit harvested the mechanical and pyroelectric energies produced by the PZT-5A sample.

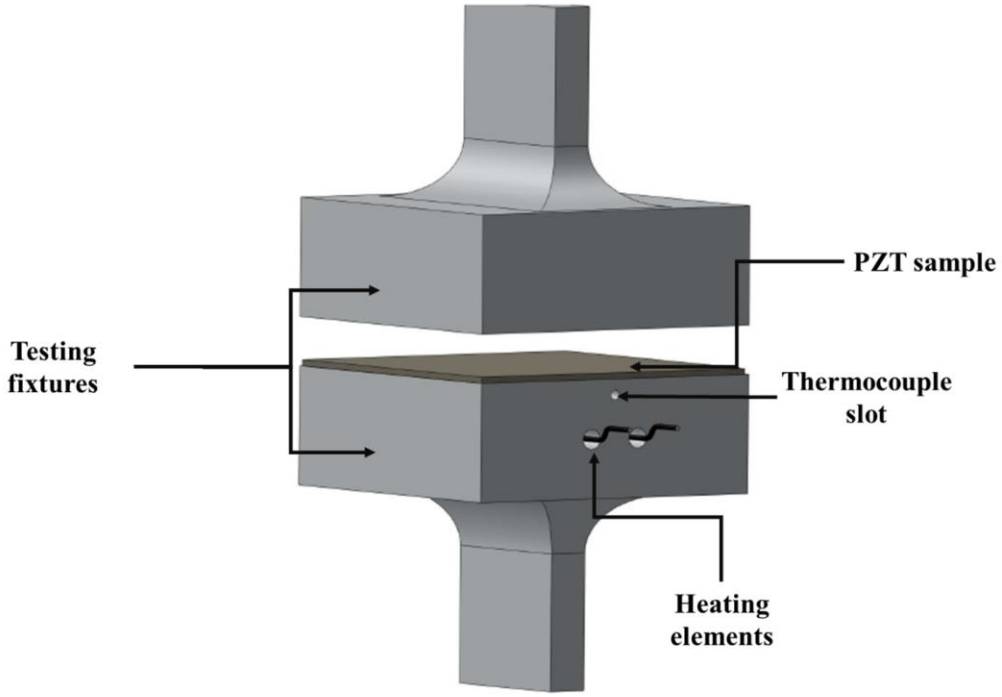

Figure 10 Finalized CAD design for custom load frame fixtures.

3.11.2 Rectifying circuit design

To harvest the energy generated by the PZT-5A sample, a parallel synchronized switch harvesting on the inductor (SSHI) rectifying circuit was constructed in house. This non-linear

method of vibration control was constructed to have the input of the rectifier bridge and the electrodes on the PZT-5A sample connected in parallel with the circuit itself. Generally a parallel SSHI circuit operates with an open switch until a voltage peak is reached on the piezoelectric component, at which point the switch closes. When open, current is able to flow through a rectifier diode bridge, however when closed current generated by the piezoelectric component flows through an inductor [84]. The peak positive voltage was directly harvested from current flowing through the inductor. Current with peak negative voltage was inverted for multiplication with this positive voltage to maximize power output. Visual representation of the constructed rectifying circuit is shown in Figure 11.

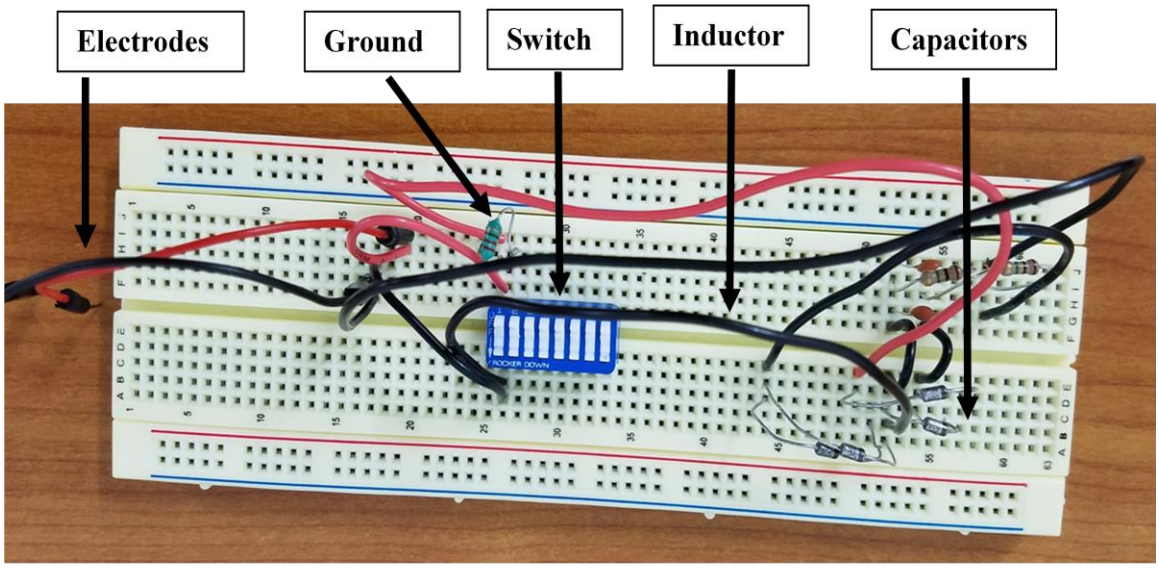

Figure 11 SSHI parallel rectifying circuit and components.

3.11.3 Load frame fixture fabrication

Due to the piezoelectric and pyroelectric nature of PZT-5A, it was desired to simultaneously apply thermal and mechanical stress to the sample for an induced charge. A custom load frame fixture capable of transferring compression-compression mechanical loads and applying thermal stresses to the sample was machined in house. This fixture was comprised of

6061 aluminum and consisted of a top and bottom component to be mounted onto an INSTRON 8801 load frame. This INSTRON load frame was capable of applying controlled amplitudes of compressional stress at various frequencies to test mechanical properties of samples. The top face of each fixture was flat and square in shape with dimensions of 50.8 mm by 50.8 mm by 25.4 mm thickness. A key feature for the bottom component of the fixture was two 1/8 inch diameter circular channels that housed 60 W resistive heating cartridges. The heating cartridges allowed for the introduction of thermal stress upon the sample via conduction. Thermal stress would be applied in cyclical heating fluctuations controlled by an Arduino Uno microcontroller and monitored by a thermocouple throughout the energy harvesting process. Load frame fixture fabrication began with original CAD file designs imported to Abaqus for finite element analysis. The feasibility of the fixture was determined through this analysis and ensured components would withstand expected combined loading conditions. The results of the FEA performed on the bottom fixture is shown in Figure 12. The finalized CAD files were then converted into a computer numerical control (CNC) language tool called a G-code file which provided automated machinery with fabrication instructions. The fixture began as a solid block of 6061 aluminum that was gradually reduced through precise machining from an automated CNC milling machine. Through guidance of the G-code file, both components emanated from the solid block and were fixated into the load frame tightly to ensure that a stationary nature was maintained throughout testing.

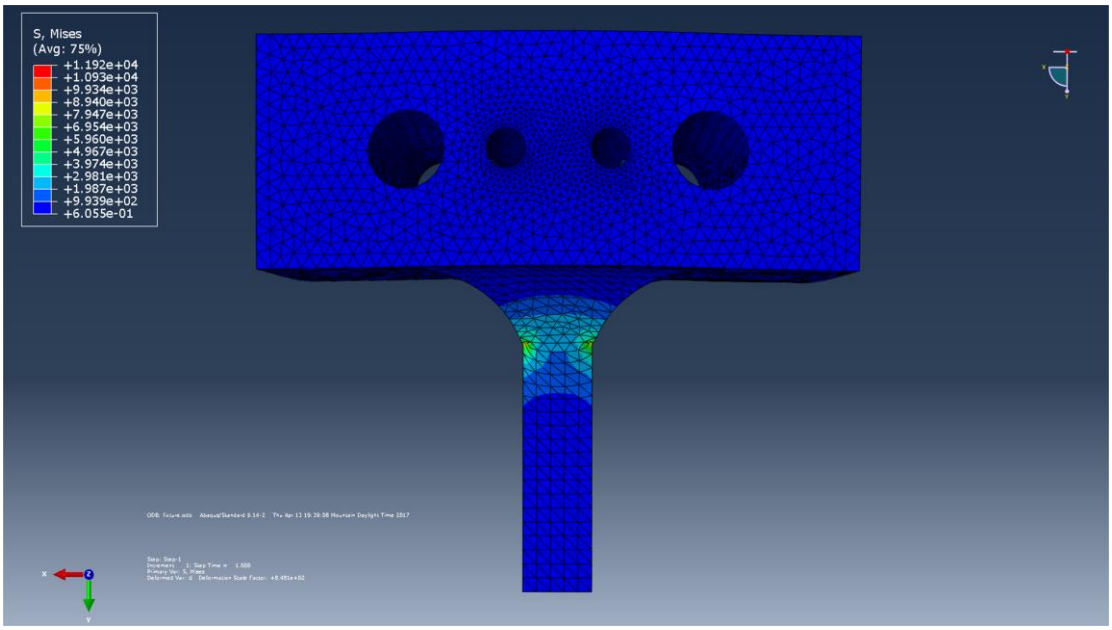

Figure 12 FEA results for bottom attachment of load frame fixture.

3.11.4 Energy harvesting testing

To determine a loading resistance that would invoke peak energy generation from the PZT-5A sample, various electrical resistors ranging from 10Ω to 10MΩ were implemented within the rectifying circuit to be tested. A Keithley 2100 digital multimeter set up to record DC voltage in the range of 10VDC was used to obtain a value for the output energy produced from the sample. This energy was a product of a current carried through the resistors to generate a voltage from excitation. Upon verifying a feasible resistance range that could potentially produce maximum power from sample excitation, energy harvesting testing conditions commenced. The first energy harvesting test method involved subjecting the PZT-5A sample to pure mechanical stress in the form of continuous compression-compression force. In order to set up the sample for mechanical testing, it was placed onto the bottom Instron load frame fixture attachment and aligned with its edges. The sample was then raised slowly until contact between the sample and top load frame fixture was made. This was confirmed when instrumentation indicated a compressional force above 1N had been applied to the sample. Once the PZT-5A was secured in the Instron load frame,

it was possible to now connect all electrical components to the sample for voltage output readings via the multimeter. The sample was then preloaded to 2500N of compression and subjected to cyclical loadings with an amplitude of 1000N with a frequency of 0.05Hz to complete the first test method. The second test method tested the pyroelectric capabilities of the sample by determining the voltage output from a pure thermal excitation. Similar to the pure mechanical test method, the sample was secured with a force of 2500N, however as opposed to being subjected to cyclical compressive loadings this test method called for the sample to be held at this force for the entire duration. Upon force application, thermal stress was then applied to the sample via heating cartridges located in the load frame fixture monitored by the Arduino microcontroller software. Temperature fluctuations ranging from 50°C to 60°C were applied to the sample in a cyclical fashion. The third and fourth testing conditions called for the cyclical mechanical loading of 1000N at a frequency of 0.05Hz previously utilized in pure mechanical testing. However prior to applying this cyclical loading, the sample was preloaded to 2500N and held to a temperature of 50°C for the third test and 60°C for the fourth test. These temperatures were held constantly for the duration of the tests. Finally for the fifth test iteration the sample was preloaded to 2500N then subjected to cyclical mechanical loading of 1000N at a frequency of 0.05Hz while simultaneously being subjected to cyclical thermal loading with temperatures ranging from 50°C to 60°C. Visual representation of the utilized test set up can be observed in Figure 13. This test method would produce a voltage output for combined loadings. These five testing methods were utilized to characterize the PZT-5A response to mechanical, thermal and combined loadings. From each test a current was created as a response from the sample being subjected to the loadings. This current generated a voltage across the varying resistance selected and was recorded for the duration of the testing process. This recorded voltage was used to determine the electrical power outputs produced by the PZT-5A sample from each testing iteration using the following equation,

Equation 10
$$P = \frac{V^2}{R}$$

where P represented the power output produced by the sample, V represented the voltage recorded from energy harvesting testing, and R represented the resistance loading applied for testing. This method of measurement as well as means of quantifying power output directly from the PZT-5A sample can be observed from Figure 14 where RL represents the varying applied electrical loading to produce optimum power and V represents the Keithley 2100 digital multimeter used to obtain a value for the generated a voltage from excitation.

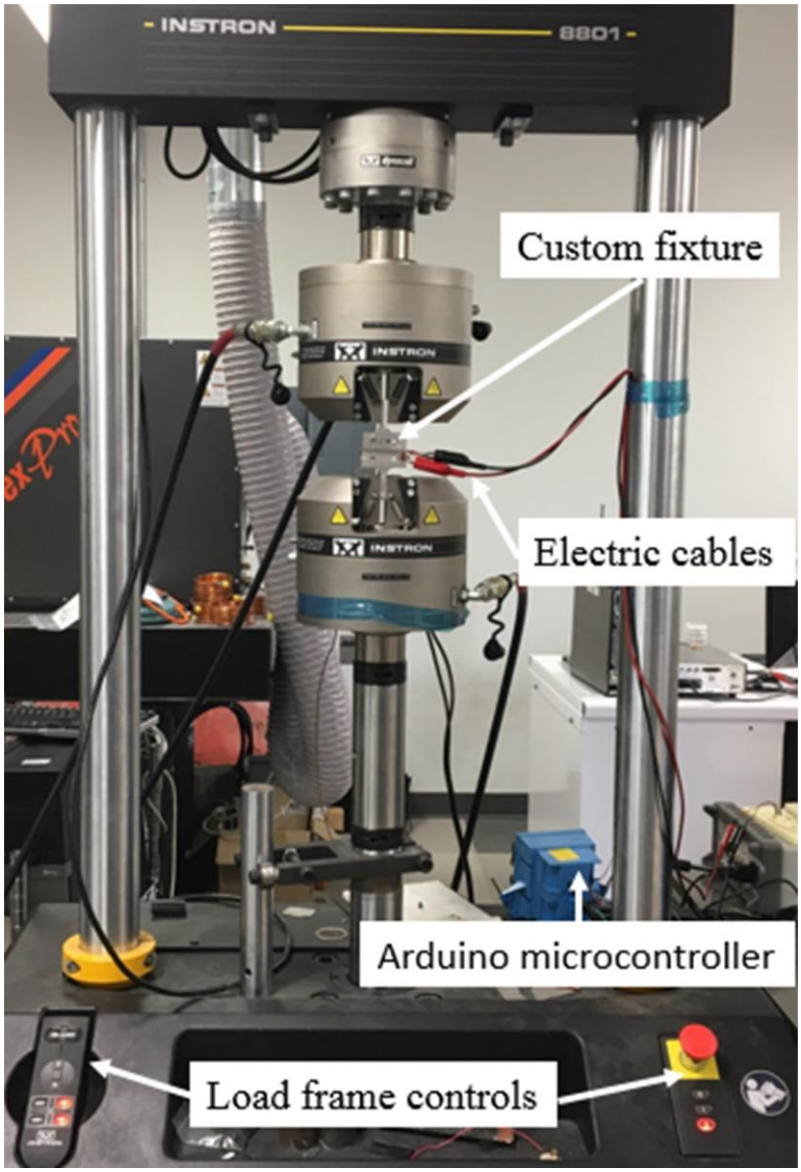

Figure 13 Load frame test set up utilized for energy harvesting testing.

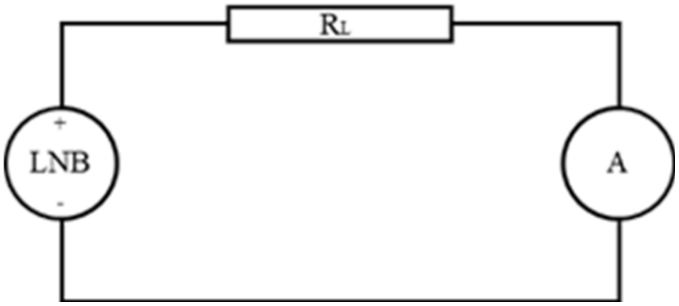

Figure 14 Schematic diagram of circuit for current and power measurement.

Chapter 4: Experimental results & discussion

4.1 BJ process parameter development

For all pure powders and their respective mixture material systems, fabrication via BJ technology was successful. Each material implemented within the ExOne M-Lab system possessed its own unique processing parameters that allowed for successful printing. For pure BTO and its mixture with PZT, the same processing parameters were used since particle size distribution for both remained approximately the same (average of 45μm). The small powder particle size of $LiNbO_3$ ($Ø_{avg}$= 8μm) on the other hand, played a role in processing parameter adjustments as particle size affected parameters such as spread speed and feed ratio. To spread this powder, a maximum spread speed of 5 mm/s was utilized and a larger feed ratio (1.90) relative to ExOne recommended standards (1.75) was implemented to ensure that an adequate supply of powder was available to spread from the feed platform to the build platform. Visual representation of printing process parameters for all materials can be observed in Table 10. Furthermore, this low spread speed and high feed ratio strategy was implemented because other work has noted a correlation between low mechanical strength in green body components and high spread speed (Miyanaji *et al.* 2016) [85]. In addition to the aforementioned powders, PZT was also successful in fabrication. While the mixture of PZT & BTO achieved the second highest AM density (57.9% TD), pure PZT components yielded the lowest and its mechanical properties did not allow for density measurements due to disintegration upon handling. The low density and inability to handle these components were attributed to the high porosity existing within the unit, which was a product of the large particle size (150 μm) of the material. Furthermore, this large powder size contributed to lager layer sizing when fabricating components which also entailed low mechanical strength.

Table 10 BJ print processing parameters.

BJ process parameters						
	Layer thickness (μm)	Powder packing rate (%)	Drying time (sec)	Spreader rapid traverse speed (mm/sec)	Desired saturation (%)	Feed powder to layer thickness ratio
Pure $LiNbO_3$	120	62.09	90	5	300	1.90
Pure BTO	45	66.02	60	15	200	1.75
Pure PZT	190	51.85	120	20	300	1.90
PZT & BTO	150	58.48	120	35	200	1.75
$LiNbO_3$ & BTO	120	63.68	90	5	200	1.90
$LiNbO_3$ & GO	120	62.09	90	5	300	1.90

Images obtained from wettability testing revealed that no iteration of the binder-GO mixture exhibited a contact angle greater than 45°. This value also revealed that the mixed solution would not repel against the surface of the powder bed and an even distribution of particles would be feasible when the two components of the mixture were brought together. Furthermore, since the angles of contact were lower than 45°, the mixture also exhibited excellent wettability throughout the AM and pellet fabrication process. Visual representation of each contact angle measurement can be observed in Figure 15.

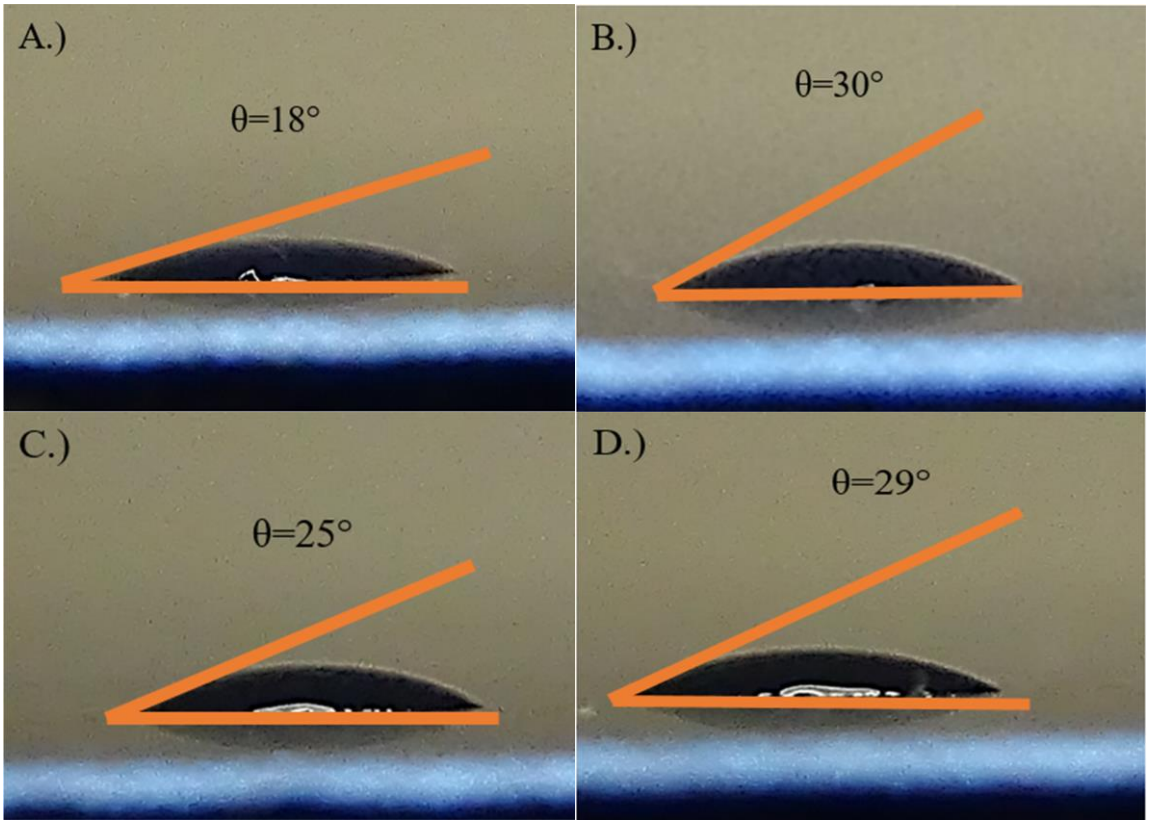

Figure 15 Contact angle of each iteration of binder. A.) Pure binder, B.) 5% weight GO, C.) 10% weight GO, D.) 15% weight GO.

4.2 Density results

The theoretical percent density of each material utilized are presented in Table 11. Upon review of density measurements amongst AM ceramic samples, the PZT &BTO material yielded the highest sintered density (57.9% TD) followed by pure BTO (43.5% TD). Pure PZT components fabricated via BJ were too porous and it was not possible to measure the density of green body or sintered samples due to disintegration. In addition to this, it was not possible to fully sinter the AM fabricated $LiNbO_3$ & GO powder due to equipment malfunctions, therefore a sintered density was not recorded. Although it was possible to lightly handle the $LiNbO_3$ & GO green body samples, the components were damaged after de-powdering and could not be sintered. It was noted that samples produced in a pellet fashion possessed greater green body and sintered density values, however provided the method of fabrication, this process was not feasible for the fabrication of

components with complex geometries. Furthermore, pellet green body samples were fabricated as a method of obtaining the highest possible density for these materials to create a baseline for comparison. Upon sintering, pellet produced samples yielded densities up to 40% higher than that of AM fabricated samples. In fact, pure $LiNbO_3$, pure BTO, and PZT & BTO pellet samples yielded 32%, 40%, and 36% higher densities than their AM fabricated counterparts, respectively.

Table 11 Density measurements for each material component iteration.

Density measurements of ceramic samples (%)				
	Pellet green body	Pellet sintered	AM green body	AM sintered
Pure $LiNbO_3$	65.6	71.4	22	39.4
Pure BTO	57.8	83.5	30.4	43.5
Pure PZT	54.7	76.5	NA	NA
PZT & BTO	56.7	94	26.1	57.9
$LiNbO_3$ & BTO	47.4	NA	NA	NA
$LiNbO_3$ & GO	55.7	57	29.1	NA

4.3 SEM & XRD

Prior to characterization of these powders, it was essential to perform scanning electron microscopy (SEM) analysis for each iteration in its pure form to obtain a better understanding of their respective characteristics. Upon analysis that can be observed in Figure 16A, pure $LiNbO_3$ revealed to be composed of several small particles which formed large agglomerates possibly formed by static electricity. The flowability of this powder was stifled by the small particles residing within the batches' size distribution as flowability is increased with larger particle sizing [86]. Similarly, in Figure 16B BTO formed agglomerates however, the consistent particle size distribution throughout the sample allowed for a powder with better spreadability characteristics. The analysis of pure PZT powder in Figure 16C appeared to reveal particle dispersion, however large agglomerations conformed in spherical formation that were comprised of several smaller particles. This allowed for a quicker flowability when compared to other aforementioned powders, however it was not considered rapid powder flowability in comparison to metal powders with a time of 15 s/50g. Finally, $LiNbO_3$ mixed with GO revealed agglomerates. In addition to this, a

broadened range of powder particle size distribution in comparison to pure $LiNbO_3$ was observed and was accredited to the implementation of GO. Visual representation of this powder iteration can be viewed in Figure 16D.

Upon sintering materials, prior to performing density measurements, SEM analysis provided an excellent indication of how near the theoretical density a component would reach. In the instance of pure BTO, it can be observed in Figure 17A that there were signs of full sintering within the examined section of the component. It was also observed however, that several voids also existed in between these small clusters of sintered sections. This porosity contributed to low mechanical strength which led to fracture upon compressional force application, deeming the component unfit for mechanical energy harvesting tests. Figure 17B reveals the poor sintering in a component comprised of pure $LiNbO_3$ as some particles appeared to be floating freely within the examined section. It can also be observed that there was a large difference in particle size between this powder and BTO. $LiNbO_3$ possessed small particles with a low range of size distribution which therefore allowed for a higher potential in void development during the layer spreading portion of the AM process. As previously mentioned, it was not possible to sinter the AM sample, therefore the sintered green body iteration of $LiNbO_3$ mixed with GO can be observed in Figure 17C. This analysis revealed that sintering does occur in small portions of the analyzed section however there were more voids present within this structure than any other. Although these voids were very small in size, a larger frequency of them populated this section of the component. Finally, SEM analysis of PZT & BTO revealed clusters of fully sintered particles beside larger voids. This sintered component possessed some positive qualities as the clusters of sintered particles were tightly packed, however voids between these clusters revealed to be in the range of 5µm-25µm in size. Nevertheless, void closure was attributed to smaller particles of BTO filling in voids left by immobile larger particles of PZT. Visual representation of the sintered particles can be observed in Figure 17D. Regardless of the positive signs of sintering observed from all SEM analysis, the issue of voids within structures remained persistent and prevented components from achieving high density. As previously mentioned, with these weak components, it was not possible to apply

any form of mechanical stress and the absence of a tight structure eventually led to the loss of piezoelectricity as well.

X-Ray diffraction (XRD) analysis revealed decomposition of PZT in AM fabricated samples from peaks in lead content. These peaks revealed the structure and composition of the sample undergoing analysis and their formation in a given diffraction pattern can best be explained by Scherrer's equation,

Equation 11
$$\tau = \frac{K\lambda}{\beta cos\theta}$$

where τ indicates the average size of crystalline domains, K represents the shape factor, λ represents the wavelength of the X-Ray scan, β represents line broadening at a fraction of the maximum intensity, and θ represents the Bragg angle. In Figure 18 XRD analysis was performed upon a pure PZT pellet sample. In this figure there was no presence of lead content from the analysis, therefore no decomposition of PZT in the sample. Furthermore, this analysis produces limited noise as a function of the limited porosity within the structure. This sample was utilized for comparison towards samples fabricated via BJ technology. In Figure 19, XRD analysis was performed upon an AM fabricated sample while searching for BTO throughout the scan. From this analysis it can be observed that the sample produced significantly more noise while also revealing barium lead oxide. The noise was attributed to the high porosity of the component whereas the barium lead oxide content revealed decomposition of the piezoelectric material. This lead oxide is a conductive material and therefore lowered the piezoelectric properties of the sample. While this analysis revealed PZT decomposition, there were several other elemental peaks present. These peaks interfered with lead peak observation therefore in Figure 20, a similar XRD scan was performed without tracing BTO. This scan maintained the noise of the previous analysis however there were far less elements present. Regardless, lead content was still revealed to be present within the sample in the form of lead titanium zirconium oxide. These traces of lead within AM fabricated samples correlated with the differing d33 measurements later recorded.

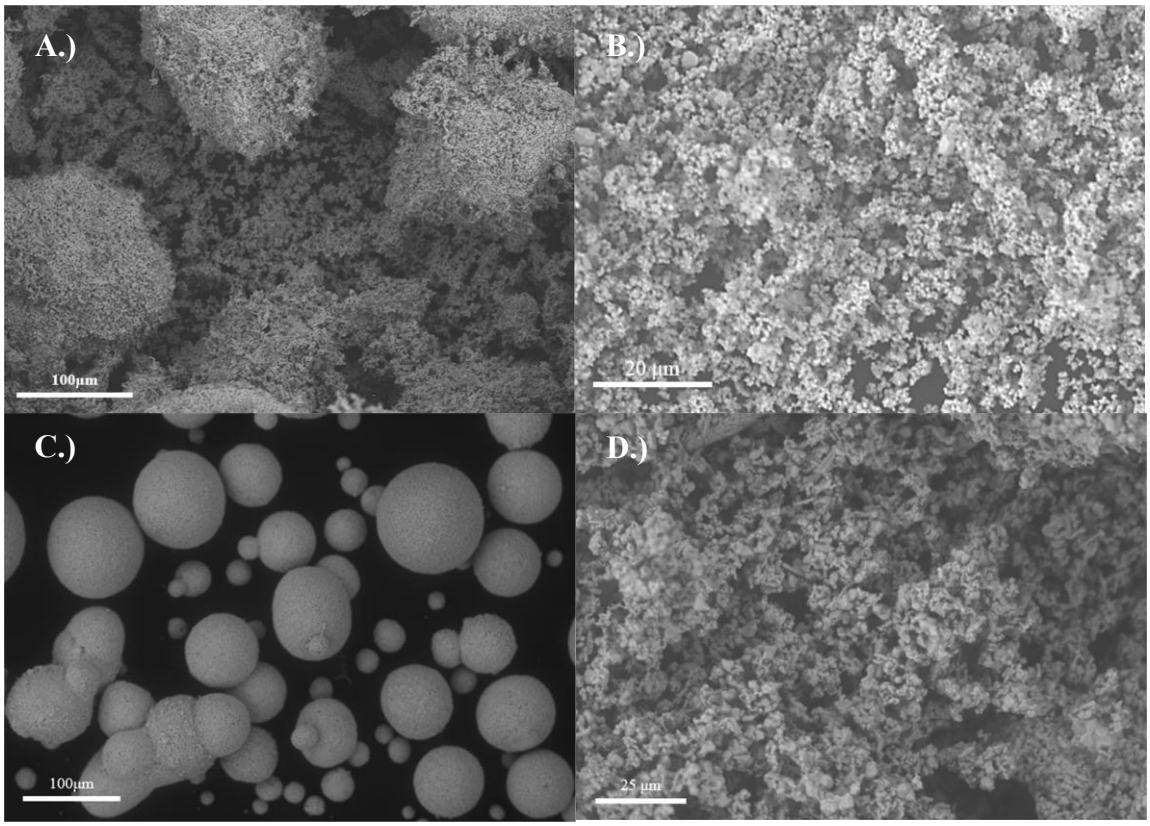

Figure 16 A.)SEM image of pure $LiNbO_3$ powder. B.) SEM image of pure BTO powder. C.) SEM image of pure PZT powder. D.) SEM image of $LiNbO_3$ & GO powder mixture.

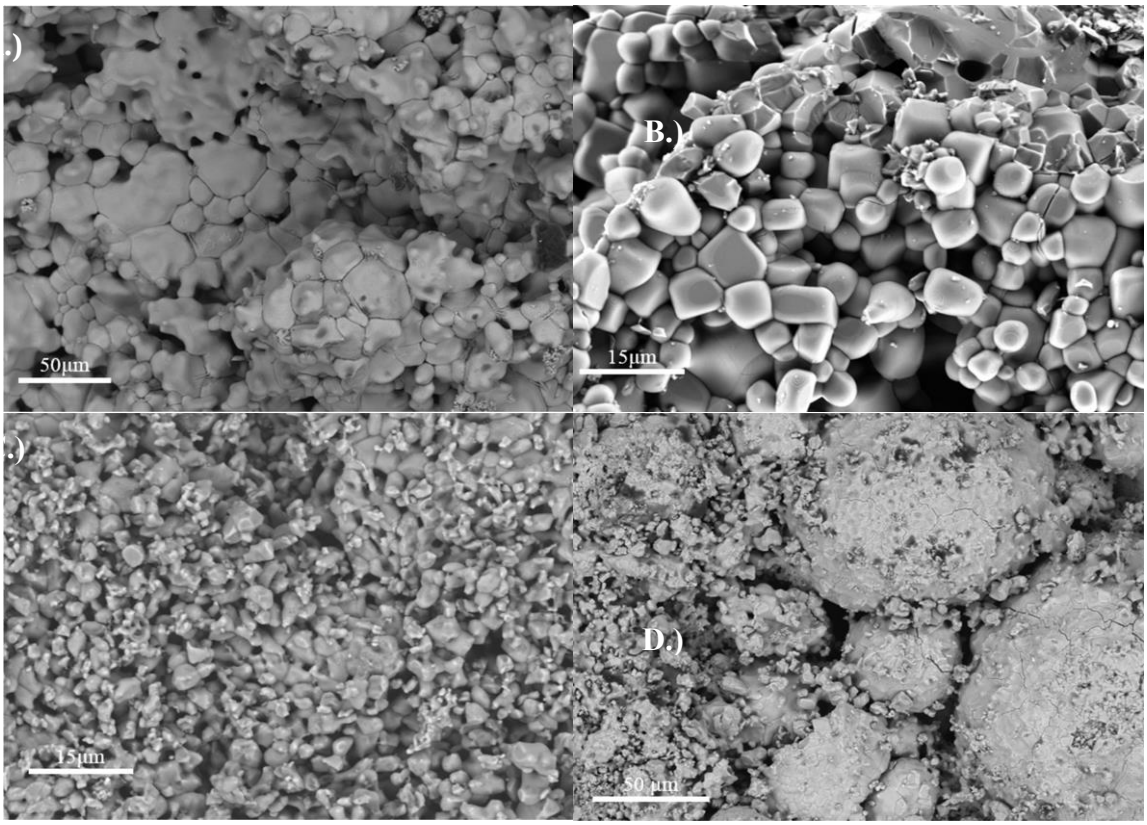

Figure 17 A.) SEM capture of BJ fabricated pure BTO sample after sintering. B.) SEM capture of pure $LiNbO_3$ after sintering. C.) SEM capture of pellet $LiNbO_3$ & GO mixture after sintering. D.) SEM capture of PZT & BTO sample after sintering.

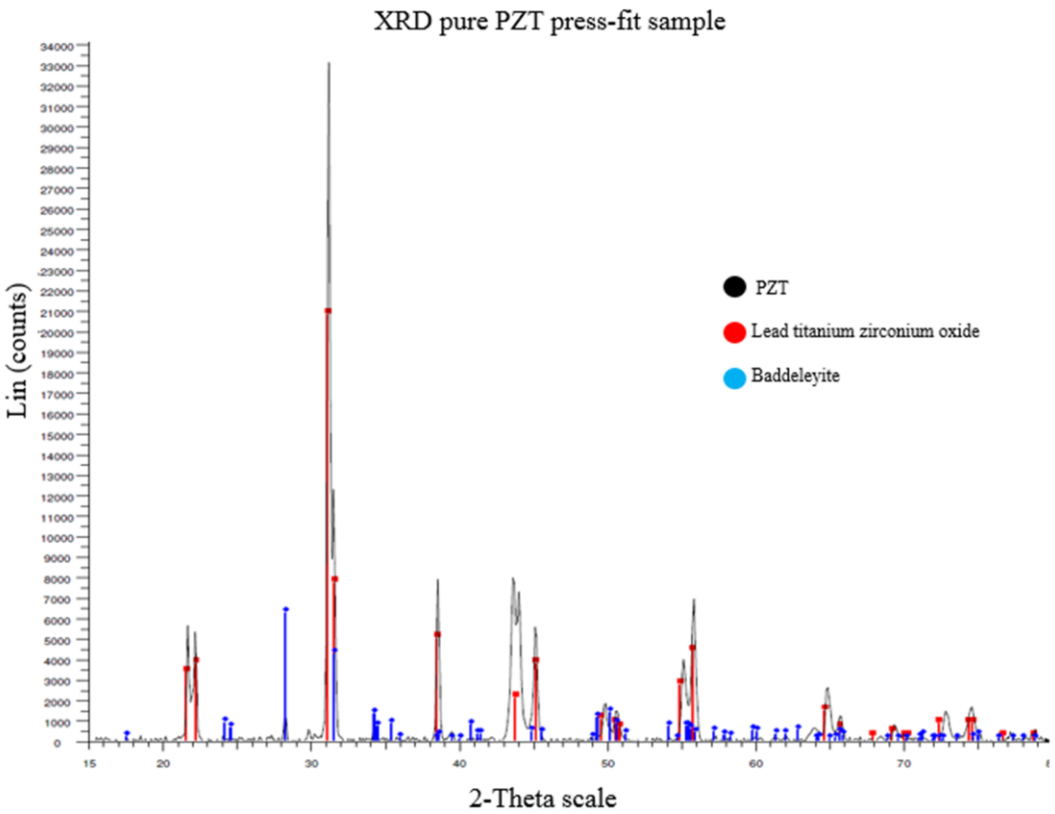

Figure 18 XRD analysis of pure PZT pellet sample.

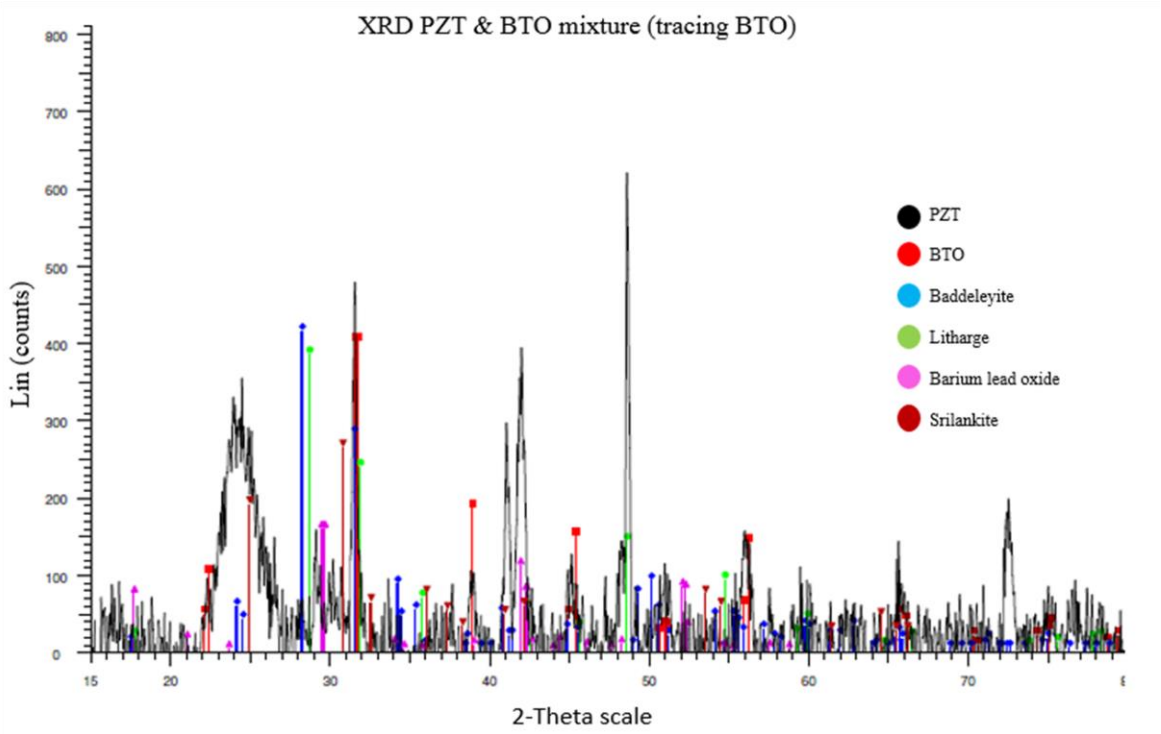

Figure 19 XRD analysis of PZT & BTO mixture searching for traces of BTO.

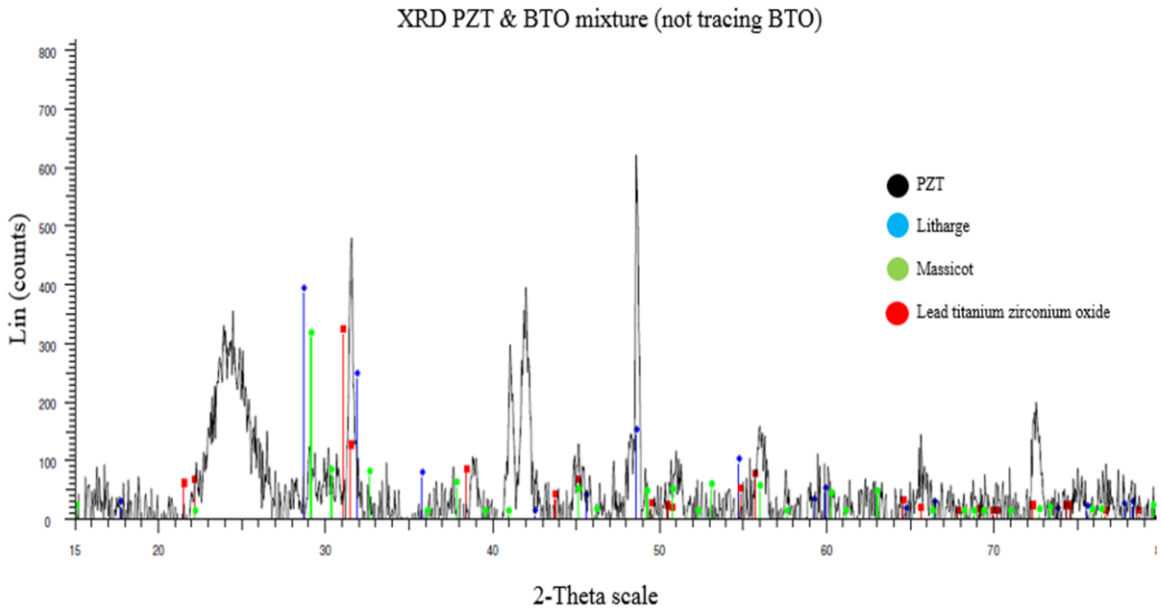

Figure 20 XRD analysis of PZT & BTO mixture not tracing BTO.

4.4 Piezoelectric property measurement

Pure BTO pellet samples mixed with concentrations of GO were fabricated prior to the AM of samples to observe the feasibility of additive implementation. Using BTO as a cost effective piezoelectric material, the addition of GO was implemented to tune the dielectric properties of the samples. Following the pellet sample fabrication method, samples containing higher concentrations of GO yielded higher dielectric results when sintered. Prior to sintering however, samples with higher concentrations of GO experienced a decreased dielectric constant. Visual representation of this can be observed in Figure 21. This phenomenon was explained by the dielectric properties of aqueous GO solution being lower than that of BTO, therefore through implementation of higher concentrations, the dielectric properties of the sample were lowered until sintered. Once sintered, the existing GO was reduced to graphene. Graphene possesses a high dielectric constant and increased the dielectric properties of samples by creating capacitors within

the component. This can be further simplified via the following mixture of dielectric constants equation,

Equation 12 $$\varepsilon_c = V_f \varepsilon_m + (1 - V_f)\varepsilon_m$$

where ε_c represents the dielectric constant of the entire component, ε_m represents the dielectric constant of the piezoelectric material matrix, and V_f represents the volume fraction dielectric constant of the additive. The highest yielded dielectric constant was possessed by a 1% GO to binder weight ratio iteration and carried a value of 575.89. Although this value did not display a significant increase in dielectric property from pure BTO, the implementation of graphene provided the desired tuning to the dielectricity of the component. Furthermore it was believed that an adequate sintering temperature had not yet been configured, as the majority of the graphene was burned out during the process.

In addition to this, pure PZT pellet samples yielded superior d33 results when subjected to measurements. These samples yielded a d33 value of 500 E^{-12}C/N on each surface after thermal poling with an electric field of 3.45Kv/mm. In conjunction to this with the same poling parameters, PZT & BTO mixture pellet samples achieved d33 measurements of 70 E^{-12}C/N. This drop in piezoelectric properties can be attributed to the lower piezoelectricity of BTO within the sample. Although the sample still contained a substantial amount of PZT, half of the component was comprised of BTO. It was not possible to acquire a sample comprised of pure PZT and fabricated via BJ that would withstand a poling process however a PZT & BTO sample mixture sample produced a d33 measurement of 3 E^{-12}C/N. This substantially lower d33 value was a product of both the lower piezoelectric properties of BTO and the high porosity within the component. Furthermore, the approach for poling these samples possibly facilitated a lower response as they were silver painted as opposed to being thermally poled.

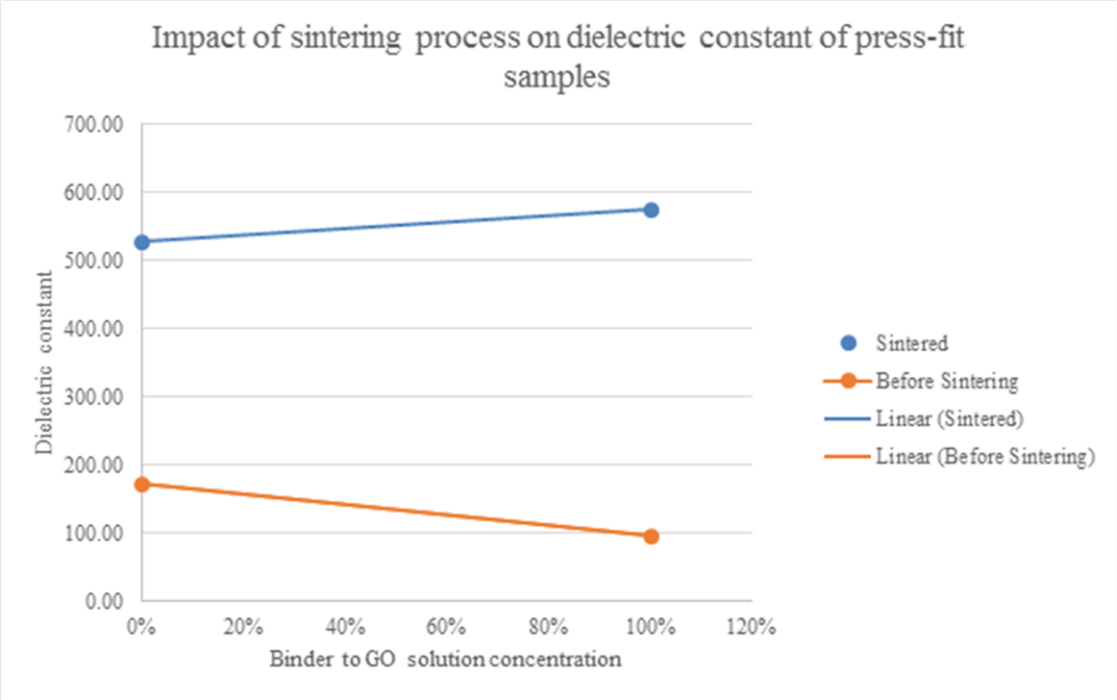

Figure 21 Dielectric constants of BTO & GO pellet samples.

4.5 Combined energy harvesting results

4.5.1 Pure mechanical loading results

Upon characterization of mechanical loading conditions, the pure mechanical loadings applied to the PZT-5A sample for responsive output voltage production are displayed in Figure 22. From this figure a peak to peak voltage of 15V produced in response a peak to peak mechanical loading of 2000N is displayed. This data coincided with the theoretical response of the sample, correlating applied stress with voltage generation, developed from material properties of PZT-5A. Although a material response from mechanical stress application was measured, an adequate indication of peak power output produced by the PZT-5A sample was further carried out by measuring voltage carried across various resistors during open circuit operation. By measuring these voltages produced from pure mechanical loading conditions it was discovered that increased resistive loadings produced higher voltages thus developing parameters for maximizing energy

harvesting capabilities. The rectified voltage output of the sample during pure mechanical testing can be observed in Figure 23. Once obtained, the voltages generated from pure mechanical excitation were used for power output calculations across each resistor. The observation made from these calculations revealed that despite voltage increasing as a function of increasing resistances, the peak power generation was recorded at a resistive loading of 10MΩ. This produced power output is displayed in Figure 24 which determined that resistive loadings in the range between 1MΩ and 100MΩ were most feasible for maximum power output. Upon further refinement, a range of resistors from 10MΩ to 60MΩ were selected for the remaining energy harvesting test conditions.

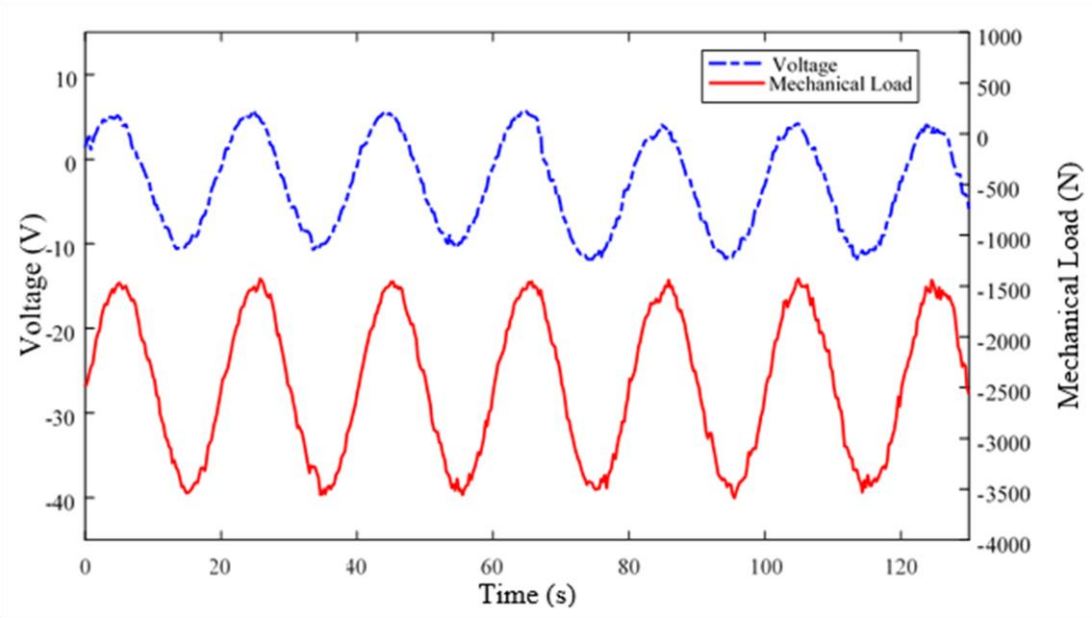

Figure 22 Voltage response to pure mechanical load application.

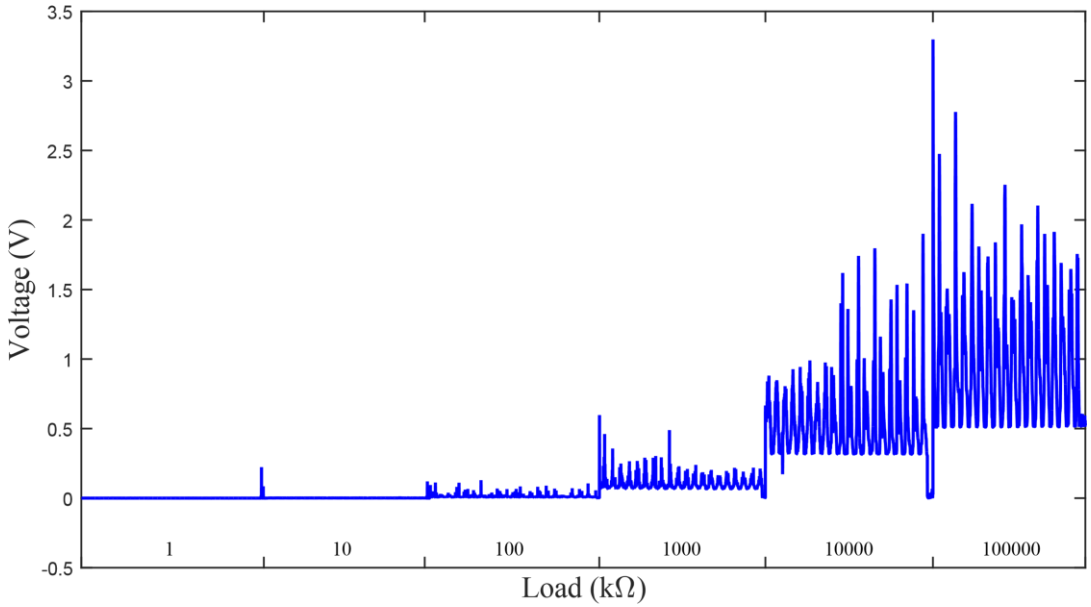

Figure 23 Rectified voltage generated from pure mechanical stress across varying resistance loadings.

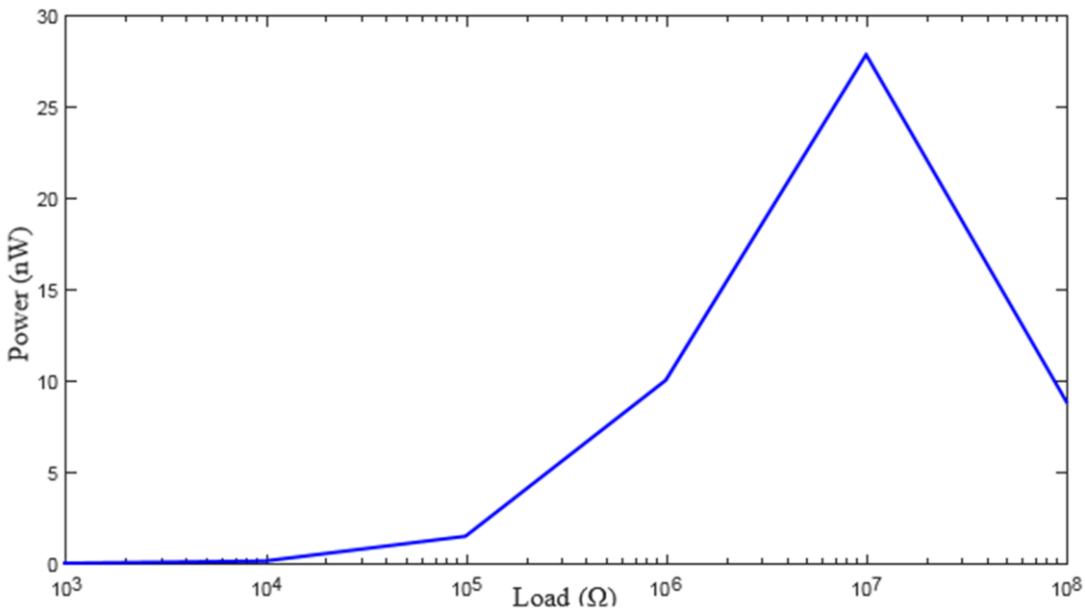

Figure 24 Power output across varying resistances upon pure mechanical loading conditions.

4.5.2 Pure thermal loading results

The sample was subjected to pure thermal cycling for a temperature range of 50°C and 60°C, producing a rectified voltage response across the aforementioned varying resistors which

can be observed in Figure 25. Beginning with a resistance of 10MΩ and augmenting to 60MΩ in increments of 10MΩ, each resistive loading condition endured 5 thermal cycles before being increased to produce a consistent voltage output for the duration of the cycling. With the average voltage output across each resistance, the power for these test parameters was calculated. Furthermore, additional testing conditions underwent the same rectifying and load changing procedure described for this process.

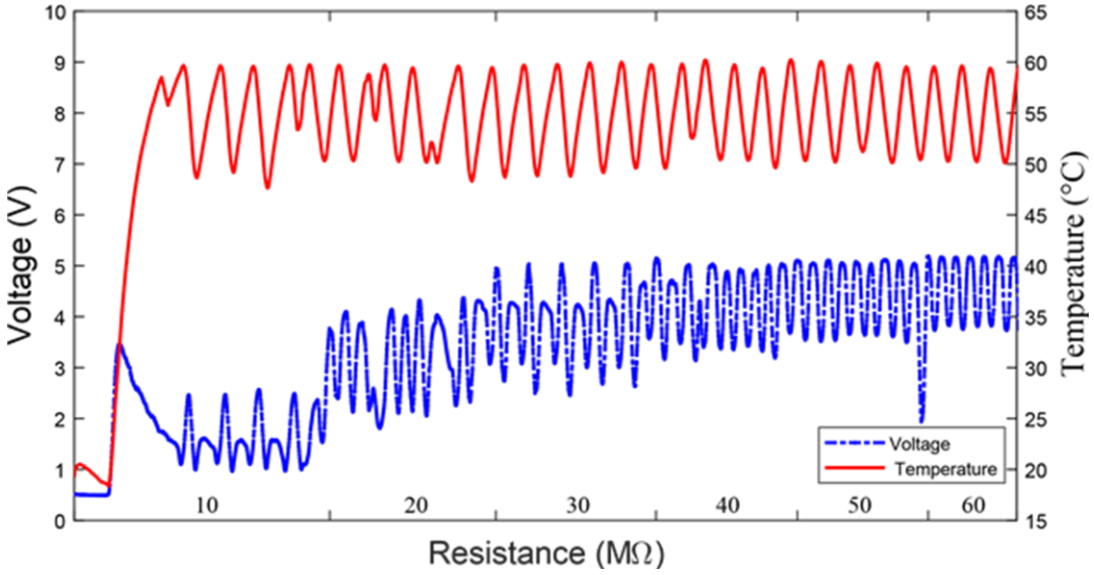

Figure 25 Voltage response from sample upon pure thermal loading application.

4.5.3 Combined loading results

For the five testing conditions that the PZT-5A sample underwent, it was determined that increased voltage output was a function of increased resistive loading conditions, however in the range of 10MΩ to 60MΩ resistance, maximum voltage output was achieved. This trend is best shown in Figure 26 where the voltage response to the five loadings across the resistance range gradually increased then began to plateau at the 50MΩ resistance. With these obtained voltage generations, the power output across each resistive loading was calculated and can be observed in Figure 27. From this figure, pure thermal loading conditions produced the highest power, followed by combined loading conditions, then mechanical loading held at 60°C, then mechanical loading held at 50°C, then finally pure mechanical loading with the lowest produced power. These thermal

results yielding the highest produced power output and increasing trend in power as a function of increased temperature revealed that thermal stress was a dominant factor in power generation from the sample. The explanation of these results emphasized the compliancy of the material to mechanical loading at higher temperatures, making strain subjected to the same mechanical loading larger. In addition to this combined loadings displayed lower power outputs regardless of higher energy applied to the sample due to electrical power outputs counteracting one another when out of phase and coming from the same source (i.e. dipole movement in the sample). Finally in Figure 27 for testing conditions that subjected the sample to more than one stress such as mechanical at 50 °C, mechanical at 60 °C, and combined loadings a second peak power output was observed. This power does not coincide with trends occurring for pure mechanical and pure thermal loading conditions and was not as immense in comparison to the maximum peak. This second peak power was attributed to the dependency of the maximum power not only to the resistive load but also to the frequency of the load being applied [86]. Furthermore, a second peak power was expected as thermal and mechanical loadings host different frequencies and were applied to the same sample.

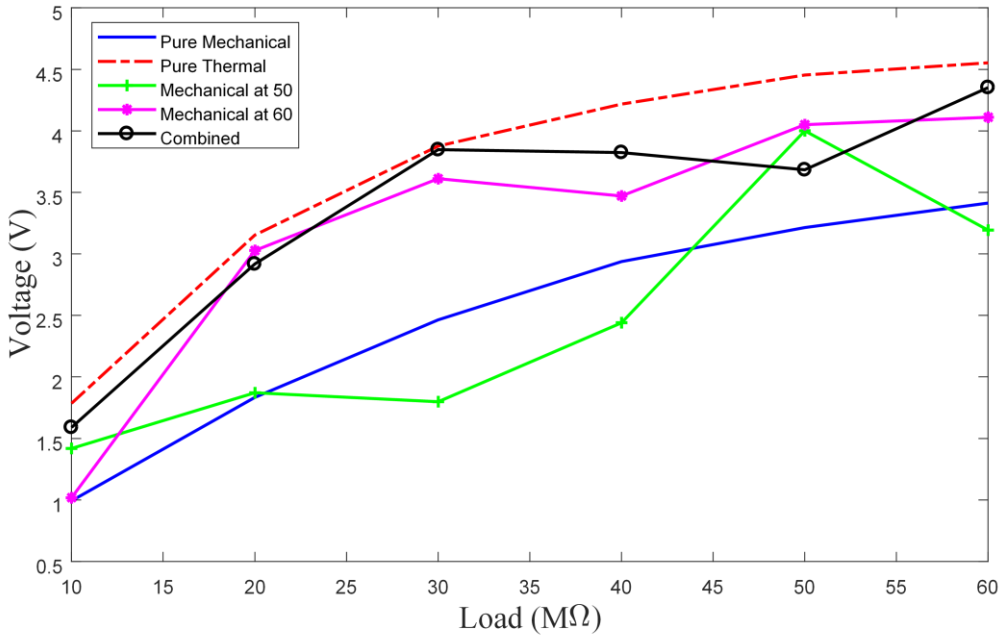

Figure 26 Voltage output of the sample for each of the five testing conditions across each resistive loading.

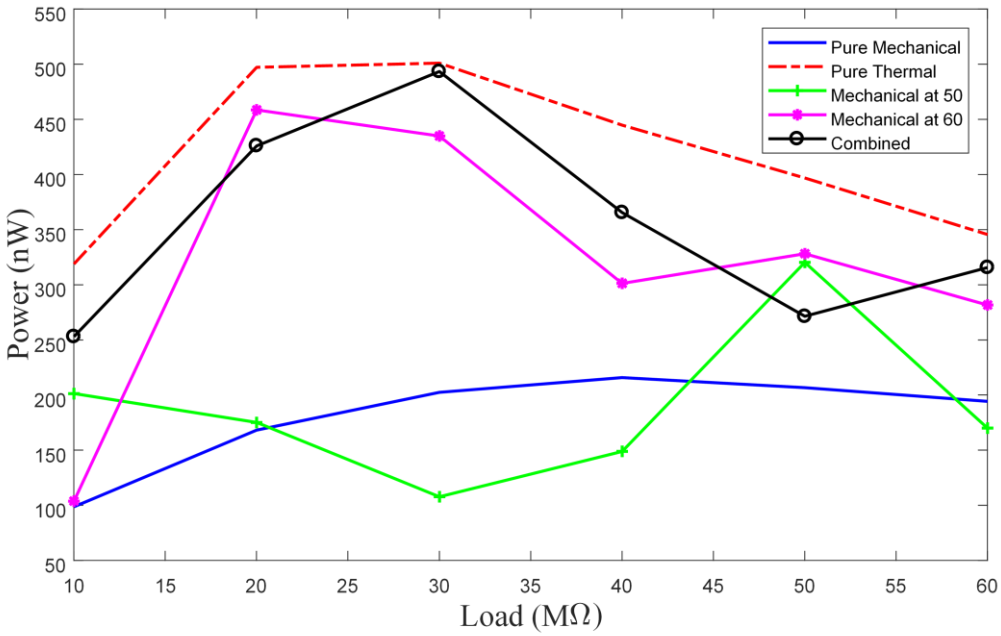

Figure 27 Power output of the sample for each of the five testing conditions across each resistive loading.

Chapter 5: Conclusions

5.1 Recommendations for future work

In the future to improve and build upon the conclusions drawn from the research conducted in the realm of fabricating ceramics via BJ technology, strategies such as parameter development for increased strength in components were some of the recommendations suggested. Lowered spread speed and increased binder saturation share a correlation with higher mechanical strength in fabricated components, therefore these parameters were subjects of interest to reach a desired density. In addition to this, materials possessing a larger powder particle size distribution can be mixed with a material of similar properties with a smaller particle size distribution to fill voids that result in porous layers. This recommendation will also assist in reducing component layer size, a function of increased mechanical strength in fabricated components. Furthermore, implementation of aqueous GO & binder mixture fully integrated within the ExOne M-lab's binder dispensing system would be a recommendation for improvement. Having this mixture travel from the binder receptacle through the print head would produce an even distribution of particles in each layer of a component throughout the fabrication process, allowing the avoidance of GO agglomerates. This can be a solution for achieving higher piezoelectric properties from AM fabricated components. Finally hot isotactic pressing (HIPing) sintered components is a costly solution for achieving a higher density from AM fabricated components. With the combination of extreme heat and high pressure, this process has shown to increase the density of ceramic components by up to 50% in research conducted withing the UTEP facility. Although costly, this process offers a solution that densifies porous structures obtained from AM fabrication, possibly bridging the gap between traditionally manufactured ceramic components and ceramics fabricated via BJ. These suggestions have direct correlation to piezoelectricity of ceramic components as higher densities have proven to yield higher d33 values.

5.2 Conclusions

PZT & BTO achieved the highest AM fabricated sintered density (57.9% TD), followed by pure BTO (43.5% TD). This was explained by smaller BTO particles being implemented within the PZT component structure, allowing smaller particle movement to fill in voids created between large PZT particles. In addition to this $LiNbO_3$ & GO green body samples yielded a higher density (29.1% TD) when compared to pure $LiNbO_3$ samples (22% TD) due to the aqueous solution eliminating static and broadening the particle size distribution existing within the pure material. Finally, it was not possible to obtain any density measurements from an AM fabricated pure PZT sample as components would disintegrate upon handling. This was due to large particle and layer size weakening the sample. An AM iteration of BTO & $LiNbO_3$ was not fabricated as a sintering reaction occurred with a preliminary pellet sample, proving that this iteration was not feasible.

Implementation of an aqueous GO solution within pure BTO pellet samples enhanced piezoelectric properties after sintering. Increased concentrations of GO within samples facilitated a higher dielectric constant however only upon sintering (575.89). Furthermore, green body samples not yet subjected to heat treatment display lowered dielectric constants (≈100) as a result of the added concentrations of GO. This was attributed to the lower dielectric constant of GO within the sample decreasing this value, then increasing this value when GO was reduced to graphene which possesses a higher dielectric constant than BTO. Although the increased dielectric properties of samples was not significant due to the majority of graphene being burned out during sintering, the presence of graphene still existing within the component proved to provide a boost in piezoelectric properties. Furthermore, it was not discovered at what temperature the component would be absolved of all binder while avoiding the burnout of graphene during the sintering process. In addition to this d33 measurements of samples containing PZT displayed similar results upon doping. Pure PZT pellet samples yield the highest d33 measurement (500 E^{-12C}/N), however when doped with BTO, this value decreased (70 E^{-12}C/N) due to the lower additive effecting the piezoelectric properties of the entire sample. Finally PZT & BTO mixture samples fabricated via

BJ technology yielded an even lower piezoelectric response (3 E^{-12}C/N) due to the heavy porosity that existed within the component.

Regarding combined energy harvesting testing, energy was indeed harvested from the PZT-5A sample. This was accomplished through material excitation via thermal and mechanical loading application both individually as well as in unison. The peak energy harvesting density was acquired during pure thermal loading application (500 nW) and a drop in power generation was observed when loadings were coupled (480 nW). This was attributed to the loading conditions being out of phase with one another causing internal counter strain within the component. Furthermore the occurrence of a second peak in power was also attributed to the various load frequencies applied to the sample. An increase in power generation as a function of increasing temperature occurred as the compliant nature of the material adheres to higher temperatures, facilitating higher mechanical strain upon the same force. Nevertheless this testing proved the feasibility of combined energy harvesting however, higher output energy was achieved solely through thermal loading application when working with PZT-5A.

Bibliography

[1] "Coal's share of global energy mix to continue rising, with coal closing in on oil as world's top energy source," 17 December 2012. [Online]. Available: https://www.iea.org/newsroom/news/2012/december/share-of-coal-in-energy-mix-to-keep-rising-nearing-oil-as-top-source-by-2017.html.

[2] ASTM International, ASTM F2792-10 Standard Terminology for Additive Manufacturing Technologies, West Conshohocken: ASTM International, 2010.

[3] B. C. Gross, J. L. Erkal, S. Y. Lockwood, C. Chen and D. M. Spence, "Evaluation of 3D Printing and Its Potential Impact on Biotechnology and the Chemical Sciences," *American Chemical Society,* vol. 18, no. 86, p. 3240−3253, 2014.

[4] X. Yan and P. Gu, "A review of rapid prototyping technologies and systems," *Computer-Aided Design,* vol. 28, no. 4, pp. 307-318, 1996.

[5] F. Ning, W. Cong, J. Qiu, J. Wei and S. Wang, "Additive manufacturing of carbon fiber reinforced thermoplastic composites using fused deposition modeling," *Composites Part B,* vol. 80, pp. 369-378, 2015.

[6] K. V. Wong and A. Hernandez, "A Review of AdditiveManufacturing," *International Scholarly Research Network,* pp. 1-10, 2012.

[7] N. Guo and M. C. Leu, "Additive manufacturing: technology, applications and research needs," *Front Mechanical Engineering,* vol. 8, no. 3, pp. 215-243, 2013.

[8] I. Campbell, D. Bourell and I. Gibson, "Additive manufacturing: rapid prototyping comes of age," *Rapid Prototyping Journal,* vol. 18, no. 4, pp. 255-258, 2012.

[9] S. Kumar and J. P. Kruth, "Composites by rapid prototyping technology," *Materials and Design,* vol. 31, pp. 850-856, 2010.

[10] Y. Yongnian , L. Shengjie, Z. Renji, L. Feng, W. Rendong, L. Qingping, X. Zhuo and W. Xiaohong, "Rapid Prototyping and Manufacturing Technology: Principle, Representative Technics, Applications, and Development Trends," *Tsinghua Science and Technology,* vol. 14, no. 1, pp. 1-12, 2009.

[11] M. Vaezi, H. Seitz and S. Yang, "A review on 3D micro-additive manufacturing technologies," *International Journal of Additive Manufacturing Technology,* vol. 67, p. 1721–1754, 2013.

[12] Y. Wang and Y. F. Zhao, "Investigation of Sintering Shrinkage in Binder Jetting Additive Manufacturing Process," *Procedia Manufacturing,* vol. 10, p. 779 – 790, 2017.

[13] S. Vangapally, K. Agarwal, A. Sheldon and S. Cai, "Effect of Lattice Design and Process Parameters on Dimensional and Mechanical Properties of Binder Jet Additively Manufactured Stainless Steel 316 for Bone Scaffolds," *Procedia Manufacturing,* vol. 10, p. 750 – 759, 2017.

[14] S. Meteyer, X. Xu, N. Perry and Y. F. Zhao, "Energy and Material Flow Analysis of Binder-jetting Additive Manufacturing Processes," *Procedia CIRP,* vol. 15, pp. 19-25, 2014.

[15] A. Kumar, Y. Bai, A. Eklund and C. B. Williams, "Effects of Hot Isostatic Pressing on Copper Parts Fabricated via Binder Jetting," *Procedia Manufacturing,* vol. 10, p. 935 – 944, 2017.

[16] ExOne Company, "Industry Grade Materials," ExOne Company, September 2015. [Online]. Available: http://www.exone.com/Resources/Materials. [Accessed 22 January 2018].

[17] M. Doyle, K. Agarwal, W. Sealy and K. Schull, "Effect of Layer Thickness and Orientation on Mechanical Behavior of Binder Jet Stainless Steel 420 + Bronze Parts," *Procedia Manufacturing,* vol. 1, p. 251–262, 2015.

[18] N. Afshar-Mohajer, C.-Y. Wu, T. Ladun, R. A. Didier and Y. Huang, "Characterization of particulate matters and total VOC emissions from a binder jetting 3D printer," *Building and Environment,* vol. 93, pp. 293-301, 2015.

[19] M. Baumers, C. Tuck, R. Hague, I. Ashcroft and R. Wildman, "A comparative study of metallic additive manufacturing power consumption," pp. 278-288, 2010.

[20] X. Xu, S. Meteyer, N. Perry and Y. F. Zhao, "Energy consumption model of Binder-jetting additive manufacturing processes," *International Journal of Production Research,* vol. 52, no. 23, p. 7005–7015, 2015.

[21] Y. Zhou, Y. Tang, T. Hoff, M. Garon and Y. F. Zhao, "The Verification of the Mechanical Properties of Binder Jetting Manufactured Parts by Instrumented Indentation Testing," *Procedia Manufacturing,* vol. 1, p. 327–342, 2015.

[22] F. Doreau, C. Chaput and T. Chartier, "Stereolithography for Manufacturing Ceramic Parts," *Advanced Engineering Materials,* vol. 2, no. 8, pp. 493-496, 2000.

[23] A. Zocca, P. Colombo, C. M. Gomes and J. Gunster, "Additive Manufacturing of Ceramics: Issues, Potentialities, and Opportunities," *The American Ceramic Society,* vol. 98, no. 7, pp. 1983-2001, 2015.

[24] Z. C. Eckel, C. Zhou, J. H. Martin, A. J. Jacobsen, W. B. Carter and T. A. Schaedler, "Additive manufacturing of polymer-derived ceramics," *Science Magazine,* vol. 351, no. 6268, pp. 58-62, 2016.

[25] Y.-C. Hagedorn, J. Wilkes, W. Meiners, K. Wissenbach and R. Poprawe, "Net Shaped High Performance Oxide Ceramic Parts by Selective Laser Melting," *Physics Procedia,* vol. 5, pp. 587-594, 2010.

[26] K. Shahzada, J. Deckers, J.-P. Kruth and J. Vleugels, "Additive manufacturing of alumina parts by indirect selective laser sintering and post processing," *Journal of Materials Processing Technology,* vol. 213, p. 1484– 1494, 2013.

[27] J. Wilkes, Y.-C. Hagedorn, W. Meiners and K. Wissenbach, "Additive manufacturing of ZrO2-Al2O3 ceramic components by selective laser melting," *Rapid Prototyping Journal,* vol. 19, no. 1, pp. 51-57, 2013.

[28] F. Niu, D. Wu, G. Ma, J. Wang, J. Zhuang and Z. Jin, "Rapid Fabrication of Eutectic Ceramic Structures by Laser Engineered Net Shaping," *Procedia CIRP,* vol. 42, pp. 91-95, 2016.

[29] J. A. Gonzalez, J. Mireles, Y. Lin and R. B. Wicker, "Characterization of ceramic components fabricated using binder jetting additive manufacturing technology," *Ceramics International,* vol. 42, no. 9, pp. 10559-10564, 2016.

[30] S. M. Gaytan, M. A. Cadena, H. Karim, D. Delfin, Y. Lin, D. Espalin, E. MacDonald and R. B. Wicker, "Fabrication of barium titanate by binder jetting additive manufacturing technology," *Ceramics International,* vol. 41, p. 6610–6619, 2015.

[31] C. B. Carter and M. G. Norton, Ceramics and Materials: Science and Engineering, New York: Springer Science+Business Media, LLC, 2007.

[32] I. W. Chen and X. H. Wang, "Sintering dense nanocrystalline ceramics without final-stage grain growth," *Nature,* vol. 404, pp. 168-171, 2000.

[33] A. Ruys, M. Wei, C. C. Sorrell, M. R. Dickson, A. Brandwood and B. K. Milthorpe, "Sintering effects on the strength of hydroxyapatite," *Biomaterials,* vol. 16, no. 5, pp. 409-415, 1995.

[34] C. Herring, "Effect of Change of Scale on Sintering Phenomena," *Journal of Applied Physics,* vol. 21, no. 301, pp. 301-303, 1950.

[35] A. R. Olszyna, P. Marchlewski and K. J. Kurzydlowski, "Sintering of high-density, high-purity alumina ceramics," *Ceramics International,* vol. 23, pp. 323-328, 1997.

[36] G. F. Fan, M. B. Shi, W. Z. Lu, Y. Q. Wang and F. Liang, "Effects of Li2CO3 and Sm2O3 additives on low-temperature sintering and piezoelectric properties of PZN-PZT ceramics," *Journal of the European Ceramic Society,* vol. 34, pp. 23-28, 2014.

[37] G. Feng, H. Rongzi, L. Jiaji, L. Zhen and T. Chang-sheng, "Effects of ZnO/Li2O codoping on microstructure and piezoelectric properties of low-temperature sintered PMN–PNN–PZT ceramics," *Ceramics International,* vol. 35, p. 1863–1869, 2009.

[38] A. Yang, C.-A. Wang, R. Guo, Y. Huang and C.-W. Nan, "Effects of sintering behavior on microstructure and piezoelectric properties of porous PZT ceramics," *Ceramics International,* vol. 36, p. 549–554, 2010.

[39] H.-I. Hsiang, C.-S. Hsi, C.-C. Huang and S.-L. Fu, "Low temperature sintering and dielectric properties of BaTiO3 with glass addition," *Materials Chemistry and Physics,* vol. 113, p. 658–663, 2009.

[40] Q. Zhang, Y. Yue, R. Nie, H. Liu, Q. Chen, P. Yu and J. Zhu, "Achieving both high d33 and high TC in low-temperature sintering Pb (Ni1/3Nb2/3)O3–Pb(Mg1/2W1/2)O3–Pb(Zr0.5Ti0.5)O3 ceramics using Li2CO3," *Materials Research Bulletin,* vol. 85, pp. 96-103, 2017.

[41] P. Figiel, M. Rozmus and B. Smuk, "Properties of alumina ceramics obtained by conventional and non-conventional methods for sintering ceramics," *Journal of Achievements in Materials and Manufacturing Engineering,* vol. 48, no. 1, pp. 29-34, 2011.

[42] K. Uchino, "The Development of Piezoelectric Materials and the New Perspective," in *Advanced Piezoelectric Materials (Second Edition)*, Pennsylvania, Woodhead Publishing Materials, 2017, pp. 1-92.

[43] H. Debéda, C. Lucat and V. Pommier-Budinger, "Printed piezoelectric materials for vibration-based damage detection," *Procedia Engineering,* vol. 168, p. 708–712, 2016.

[44] G. Martínez-Ayuso, M. I. Friswell, S. Adhikari, H. Haddad Khodaparast and H. Berger, "Homogenization of porous piezoelectric materials," *International Journal of Solids and Structures,* Vols. 113-114, p. 218–229, 2017.

[45] A. Erturk and D. J. Inman, "Pizoelectric energy harvesting," John Wiley & Sons, 2011.

[46] K. Viswanath Allamraju and K. Srikanth, "State of art: Piezoelectric Vibration Energy Harvesters," *Materials Today: Proceedings,* vol. 4, p. 1091–1098, 2017.

[47] M. T. Todaro, F. Guido, V. Mastronardi, D. Desmaele, G. Epifani, L. Algieri and M. De Vittorio, "PiezoelectricMEMS vibrational energy harvesters: Advances and outlook," *Microelectronic Engineering,* Vols. 183-184, pp. 23-36, 2017.

[48] K. Uchino, "Piezoelectric Composite Materials," in *Advanced Piezoelectric Materials*, State college, Woodhead Publishing, 2010, p. 318–346.

[49] P. K. Panda, "Review: environmental friendly lead-free piezoelectric materials," *Journal of Materials Science,* vol. 44, p. 5049–5062, 2009.

[50] S. J. Zhang, F. Li and F. P. Yu, "Piezoelectric materials for cryogenic and high-temperature applications," in *Structural Health Monitoring (SHM) in Aerospace Structures*, University Park, Woodhead Publishing, 2016, pp. 59-93.

[51] S. R. Anton and H. A. Sodano, "A review of power harvesting using piezoelectric materials (2003–2006)," *Smart Materials and Structures,* vol. 16, no. 1, pp. R1-R21, 2007.

[52] S. Dalola, V. Ferrari and D. Marioli, "Pyroelectric Effect in PZT Thick Films for Thermal Energy Harvesting in Low-Power Sensors," *Procedia Engineering,* vol. 5, p. 685–688, 2010.

[53] S. B. Riffat and X. Ma, "Thermoelectrics: a review of present and potential applications," *Applied Thermal Engineering,* vol. 23, pp. 913-935, 2003.

[54] F. Y. Lee, A. Navid and L. Pilon, "Pyroelectric waste heat energy harvesting using heat conduction," *Applied Thermal Engineering,* vol. 37, pp. 30-37, 2012.

[55] G. Sebald, D. Guyomar and A. Agbossou, "On thermoelectric and pyroelectric energy harvesting," *Smart Materials and Structures,* vol. 18, pp. 1-8, 2009.

[56] V. Ferrari, A. Ghisla, D. Marioli and A. Taroni, "Array of PZT Pyroelectric Thick-Film Sensors for Contactless Measurement of XY Position," *Sensors,* pp. 889-894, 2002.

[57] H. Karim, M. R. H. Sarker, S. Shahriar, M. A. I. Shuvo, D. Delfin, D. Hodges, T.-L. Tseng, D. Roberson, N. Love and Y. Lin, "Feasibility study of thermal energy harvesting using lead free pyroelectrics," *Smart Materials and Structures,* vol. 25, pp. 1-8, 2015.

[58] C. R. Bowen, J. Taylor, E. LeBoulbar, D. Zabek, A. Chauhan and R. Vaish, "Pyroelectric materials and devices for energy harvesting applications," *Energy & Environmental Science,* vol. 7, no. 12, p. 3817–4148, 2014.

[59] A. Cuadras, M. Gasulla and V. Ferrari, "Thermal energy harvesting through pyroelectricity," *Sensors and Actuators A: Physical,* vol. 158, p. 132–139, 2010.

[60] Q. Zhang, A. Agbossou, Z. Feng and M. Cosnier, "Solar micro-energy harvesting with pyroelectric effect and wind flow," *Sensors and Actuators A: Physical,* vol. 168, p. 335–342, 2011.

[61] F. Z. El Fatnani, D. Guyomar, M. Mazroui, F. Belhora and Y. Boughaleb, "Optimization and improvement of thermal energy harvesting by using pyroelectric materials," *Optical Materials,* vol. 56, pp. 22-26, 2016.

[62] I. Stark, "Thermal Energy Harvesting with Thermo Life," in *Proceedings of the International Workshop on Wearable and Implantable Body Sensor Networks*, Riverside, 2006.

[63] C. R. Bowen, J. Taylor, E. L. Boulbar, D. Zabek and V. Y. Topolov, "A modified figureof merit for pyroelectric energy harvesting," *Materials Letters,* vol. 138, pp. 243-246, 2015.

[64] J. Rastegar, C. Pereira and H. L. Nguyen, "Piezoelectric-based power sources for harvesting energy from platforms with low-frequency vibration," *Proceedings of SPIE,* vol. 6171, pp. 1-8, 2006.

[65] C. A. Howells, "Piezoelectric energy harvesting," *Energy Conversion and Management,* vol. 50, p. 1847–1850, 2009.

[66] Y. Liao and A. Sodano, "Model of a single mode energy harvester and properties for optimal power generation," *Smart Materials and Structures,* vol. 17, no. 6, pp. 1-15, 2008.

[67] K. A. Cook-Chennault, N. Thambi and A. M. Sastry, "Powering MEMS portable devices—a review of non-regenerative and regenerative power supply systems with special emphasis on piezoelectric energy harvesting systems," *Smart Materials and Structures,* vol. 17, pp. 1-33, 2008.

[68] Q. M. Wang and L. E. Cross, "Constitutive equations of symmetrical triple layer piezoelectric benders," *IEEE Transactions on Ultrasonics, Ferroelectrics, and Frequency Control,* pp. 1343-1351, 1999.

[69] M. Lumentut and I. Howard, "Intrinsic electromechanical dynamic equations for piezoelectric power harvesters," *Acta Mechanica,* pp. 631-650, 2017.

[70] H. Shen, J. Qiu and M. Balsi, "Vibration damping as a result of piezoelectric energy harvesting," *Sensors and Actuators A: Physical,* vol. 169, pp. 178-186, 2011.

[71] X. Chen, S. Xu, N. Yao and Y. Shi, "1.6 V Nanogenerator for Mechanical Energy Harvesting Using PZT Nanofibers," *Nano Letters,* vol. 10, p. 2133–2137, 2010.

[72] G. A. Lesieutre, G. K. Ottman and H. F. Hofmann, "Damping as a result of piezoelectric energy harvesting," *Journal of Sound and Vibration,* vol. 269, p. 991–1001, 2004.

[73] H. A. Sodano, G. Park and D. J. Inman, "Estimation of Electric Charge Output for Piezoelectric Energy Harvesting," *Strain,* vol. 40, pp. 49-58, 2004.

[74] M. N. Fakhzan and A. G. Muthalif, "Harvesting vibration energy using piezoelectric material: Modeling, simulation and experimental verifications," *Mechatronics,* vol. 23, pp. 61-66, 2013.

[75] R. R. Romanosky and S. M. Maley, "Harsh environment sensor development for advanced energy systems," *Proceedings of SPIE,* vol. 8725, pp. 1-9, 2013.

[76] S. Priya and D. J. Inman, Energy Harvesting Technologies, Boston: Springer, 2009.

[77] V. Leonov, "Thermoelectric Energy Harvesting of Human Body Heat for Wearable Sensors," *IEEE Sensors Journal,* pp. 2284-2291, 2013.

[78] J. Fang, H. Niu, H. Wang, X. Wang and T. Lin, "Enhanced mechanical energy harvesting using needleless electrospun poly(vinylidene fluoride) nanofibre webs," *Energy & Environmental Science,* pp. 2196-2202, 2013.

[79] C. Alippi and C. Galperti, "An Adaptive System for Optimal Solar Energy Harvesting in Wireless Sensor Network Nodes," *IEEE Transactions on Circuits and Systems,* pp. 1742-1750, 2008.

[80] R. W. Whatmore, "Pyroelectric devices and materials," *Reports on Progress in Physics,* vol. 49, pp. 1335-1386, 1986.

[81] S. Bandyopadhyay and A. P. Chandrakasan, "Platform Architecture for Solar, Thermal, and Vibration Energy Combining With MPPT and Single Inductor," *IEEE Journal of Solid-State Circuits,* vol. 47, no. 9, pp. 2199-2215, 2012.

[82] ASTM International, Standard Practice for Surface Wettability of Coatings, Substrates and Pigments by Advancing Contact Angle Measurement, West Conshohocken: ASTM International, 2013.

[83] ASTM International, ASTM B213-17 Standard Test Methods for Flow Rate of Metal Powders Using the Hall Flowmeter Funnel, West Conshohocken: ASTM International, 2017.

[84] L. Mateu, L. LUhmann, H. Zessin and P. Spies, "Modified Parallel SSHI AC-DC Converter for Piezoelectric Energy Harvesting Power Supplies," *Telecommunications Energy Conference (INTELEC),* vol. 33, pp. 1-7, 2011.

[85] H. Miyanaji, S. Zhang, A. Lassell, A. A. Zandinejad and L. Yang, "Optimal Process Parameters for 3D Printing of Porcelain Structures," *Procedia Manufacturing,* vol. 5, pp. 870-887, 2016.

[86] L. X. Liu, I. Marziano, A. C. Bentham, J. D. Lister, E. T. White and T. Howes, "Effect of particle properties on the flowability of ibuprofen powders," *International Journal of Pharmaceutics,* vol. 362, no. 1-2, pp. 109-117, 2008.

[87] N. Kong, D. S. Ha, A. Erturk and D. J. Inman, "Resistive impedance matching circuit for piezoelectric energy harvesting," *Journal of Intelligent Material Systems and Structures,* vol. 21, no. 13, pp. 1293-1302, 2010.

[88] M. Doyle, K. Agarwal, W. Sealy and K. Schull, "Effect of Layer Thickness and Orientation on Mechanical Behavior of Binder Jet Stainless Steel 420 + Bronze Parts," *Procedia Manufacturing,* vol. 1, pp. 251-262, 2015.

Vita

Victor Fernando Elicerio was born on November 5, 1992 to Fernando and Julissa Elicerio. Victor obtained his high school diploma from Americas high school in 2011 and his Bachelor of Science in Mechanical Engineering degree in the spring of 2016. During the time of his graduate career, Victor worked as a research assistant for the W.M. Keck center for 3D Innovation, Csetr and teachers assistant for the mechanical engineering department at The University of Texas at El Paso. In addition to this he worked as an AM intern at Edison Welding Institute in Buffalo, New York. Victor also assisted students, provided lab tours, and presented research at the U.S. Department of energy project review meeting for crosscutting research, gasification systems, and rare earth elements.

Email address: vfelicerio@miners.utep.edu

This thesis/dissertation was typed by Victor Fernando Elicerio.